DOE award #: SC0004162

Name of the recipient (Institution): Yale University

Project Title: Dynamics of Block Copolymer Nanocomposites

Lead PI: Simon Mochrie

Business Mailing Address: SPL 68C, 217 Prospect Ave., New Haven, CT 06511

Telephone Number: (203) 436 4809

Email: simon.mochrie@yale.edu

Period covered by the report: 6/1/2010-5/31/2014

Abstract:

A detailed study of the dynamics of cadmium sulfide nanoparticles suspended in polystyrene homopolymer matrices was carried out using X-ray photon correlation spectroscopy for temperatures between 120 and 180 °C. For low molecular weight polystyrene homopolymers, the observed dynamics show a crossover from diffusive to hyper-diffusive behavior with decreasing temperatures. For higher molecular weight polystyrene, the nanoparticle dynamics appear hyper-diffusive at all temperatures studied. The relaxation time and characteristic velocity determined from the measured hyper-diffusive dynamics reveal that the activation energy and underlying forces determined are on the order of 2.14×10^{-19} J and 87 pN, respectively. We also carried out a detailed X-ray scattering study of the static and dynamic behavior of a styrene–isoprene diblock copolymer melt with a styrene volume fraction of 0.3468. At 115 and 120 °C, we observe splitting of the principal Bragg peak, which we attribute to phase coexistence of hexagonal cylindrical and cubic double- gyroid structure. In the disordered phase, above 130 °C, we have characterized the dynamics of composition fluctuations via X-ray photon correlation spectroscopy. Near the peak of the static structure factor, these fluctuations show stretched-exponential relaxations, characterized by a stretching exponent of about 0.36 for a range of temperatures immediately above the MST. The corresponding characteristic relaxation times vary exponentially with temperature, changing by a factor of 2 for each 2 °C change in temperature. At low wavevectors, the measured relaxations are diffusive with relaxation times that change by a factor of 2 for each 8 °C change in temperature.

Keywords: x-ray photon correlation spectroscopy, nanoparticles, nanocomposites, block copolymers

Publications:

(1) W.-S. Jang, P. Koo, M. Sykorsky, S. Narayanan, A. Sandy, S. G. J Mochrie, “The Static and Dynamic Structure Factor of a Diblock Copolymer Melt via Small-Angle X-ray Scattering and X-ray Photon Correlation Spectroscopy”,

Macromolecules 46, 8628-8637 (2013) DOI 10.1021/ma4014548
(2) W.-S. Jang, P. Koo, K. Bryson, S. Narayanan, A. Sandy, T. P. Russell, S. G. J. Mochrie, “Dynamics of Cadmium Sulphide Nanoparticles within Polystyrene Melts” Macromolecules in press (2014) DOI 10.1021/ma500956b.

Report:

Comprehensive reports of the outcomes of this project have appeared in the two publications in Macromolecules:

Macromolecules

Article

pubs.acs.org/Macromolecules

Dynamics of Cadmium Sulfide Nanoparticles within Polystyrene Melts

Woo-Sik Jang,*[,†,⊥] Peter Koo,[†] Kyle Bryson,[‡] Suresh Narayanan,[§] Alec Sandy,[§] Thomas P. Russell,[‡] and Simon G. Mochrie*[,†]

[†]Department of Physics, Yale University, 217 Prospect Street, Sloane Physics Lab, New Haven, Connecticut 06511, United States

[‡]Department of Polymer Science and Engineering, University of Massachusetts Amherst, 120 Governors Drive, Amherst, Massachusetts 01003-9263, United States

[§]Advanced Photon Source, Argonne National Laboratory, 9700 South Cass Avenue, Sector 8, Building 432E, Argonne, Illinois 60439, United States

Supporting Information

ABSTRACT: We present a detailed study of the dynamics of cadmium sulfide nanoparticles suspended in polystyrene homopolymer matrices using X-ray photon correlation spectroscopy for temperatures between 120 and 180 °C. For low molecular weight polystyrene homopolymers, the observed dynamics show a crossover from diffusive to hyper-diffusive behavior with decreasing temperatures. For higher molecular weight polystyrene, the nanoparticle dynamics appear hyper-diffusive at all temperatures studied. The relaxation time and characteristic velocity determined from the measured hyper-diffusive dynamics reveal that the activation energy and underlying forces determined are on the order of 2.14×10^{-19} J and 87 pN, respectively.

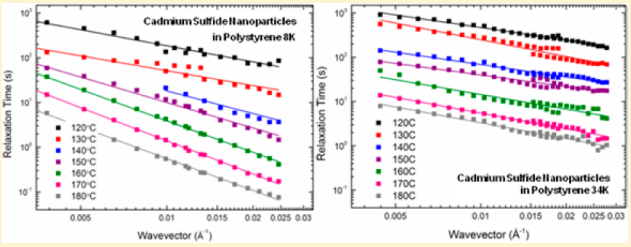

INTRODUCTION

Polymeric materials are used in a huge variety of products as a result of their many convenient properties, including that they are lightweight, inexpensive, and easily formed. However, conventional polymers lack many desirable properties that are commonly found in inorganic or metallic materials. Recently, the desire to incorporate such properties into polymeric materials has driven the introduction of polymer nanocomposites materials, in which inorganic or metallic nanoparticles (NPs) are incorporated into a polymeric matrix. Polymer nanocomposites can be expected to display a combination of the properties of their parent polymeric and inorganic or metallic components. Already, such material design flexibility has been used to create materials for oxygen barriers,[1] flexible displays,[2] light emitting diodes,[3] thermoelectric materials,[4] optical sensors,[5] electric storage,[6] solar cells,[7] and magnetic storages.[8] A promising class of nanocomposites consists of dispersions of semiconductor NPs within a polymeric matrix, where the particles' interaction with the matrix may provide a means to precisely control the nanostructure.[9−12] These semiconductor NPs in the 2 to 50 nm size regime exhibit unique electromagnetic[13,14] and optical[13−16] properties which can be applicable to modern organic and inorganic light-emitting diodes.[17,18]

Over the past decade, a variety of approaches for fabricating semiconductor NPs using the unique structure of block copolymers have been developed. Several research groups have prepared metal/semiconductor NPs in poly(styrene-*b*-2 vinylpyridine) (S2VP) or poly(styrene-*b*-4 vinylpyridine) (S4VP) which are solvent-selective micellar diblock copolymers.[19−25] In chloroform or toluene, the soluble polystyrene (PS) block forms a shell around the insoluble 2 or 4 vinylpyridine core. Because 2 and 4 vinylpyridine are strong metal-chelating agents,[23,26] metal ions can become incorporated within the core to form metal-based NPs. Specifically, Cd^{2+} ions are precipitated with gaseous hydrogen sulfide (H_2S)[19,20,27−30] or mixed with sodium sulfide (Na_2S) in aqueous solutions.[24,25,31−35] For the aqueous-based synthesis technique, subsequent mixing of Na_2S solution creates the corresponding cadmium sulfide (CdS) or other metal sulfide NPs. The resultant S2VP or S4VP core-embedded CdS NPs are decorated by the styrene shells.

Despite of a tremendous amount of work on the fabrication and characterization of semiconductor NPs, the structural dynamics of these materials remain poorly understood. Recently, the dynamics of NPs within aqueous suspensions[36−39] or polymeric matrices[40−42] have been studied with dynamic light scattering (DLS). However, the length scales that are accessed by light scattering techniques are in the range of ∼500 nm or greater. By contrast, X-ray photon correlation spectroscopy (XPCS)[43] can access length scales ∼20 nm and larger, which is in the appropriate size of individual NPs. XPCS

Received: May 9, 2014
Revised: August 21, 2014

   dx.doi.org/10.1021/ma500956b | *Macromolecules* XXXX, XXX, XXX−XXX

measures the time autocorrelation function of the small-angle X-ray scattering (SAXS) intensity: $I(q, t)$:

$$g_2(q, t_d) \equiv \frac{\langle I(q, 0)\cdot I(q, t_d)\rangle}{\langle I(q, 0)\rangle^2} \quad (1)$$

The correlation function, g_2, decays with increasing delay time, t_d, and converges to unity at long times. Because of the large X-ray contrast between polymer and NPs, the characteristic decay time (τ) reflects the dynamic behavior of the NPs within the suspending medium. To determine the characteristic relaxation times, we represent eq 1 with the following form:

$$g_2(q, t_d) = 1 + A[g_1(q, t_d)]^2 \quad (2)$$

Here A is the speckle contrast and $g_1(q,t_d) = \exp[-((t_d/\tau)^{\beta})]$ is the intermediate scattering function (ISF). XPCS measurements are performed as described elsewhere[44] and the resultant intensity autocorrelation functions are fit using either a simple ($\beta = 1$), stretched ($0 < \beta < 1$), or compressed ($\beta > 1$) exponential forms for the ISF.

Slow relaxations are ubiquitous in disordered condensed matter systems including supercooled liquids,[45] polymer melts,[46] colloidal gels,[47−50] clay suspensions,[51,52] emulsions,[53,54] and inorganic or metallic NPs within polymeric matrix.[55] These dynamics frequently display aging.[50,51,55] Typical behavior of aging is an increase in the characteristic relaxation time with increasing aging time. Guo et al. investigated the motion of dilute suspensions of gold (Au) NPs in two different molecular weight (M_W = 2000 and 13000 g/mol) PS melts via XPCS and presented the aforementioned slow relaxation and aging.[55] Moreover, these disordered condensed matter systems exhibit peculiar crossover behavior and hyper-diffusive dynamics.[46−48,50,55] Two concepts have been presented to account for hyper-diffusive dynamics. One is a continuous time random walk (CTRW).[48,56] For CTRW, β depends on the distribution of the particle jump size at small q. At large q, CTRW predicts a q-independent relaxation time. The other is stress-field relaxation[47,50,57] which gives $\beta \cong 1.5$ and $\tau \sim q^{-1}$ but has no intrinsic length scale. The former is suitable to explain the wavevector dependence of crossover behavior while the latter is more adequate to describe temperature dependence of crossover behavior.

Here, we present a comprehensive experimental study of structure and dynamics of CdS NPs; henceforth, CdS−S2VPs, within low (8 kg/mol) and intermediate (34.3 kg/mol) molecular weight PS matrices. At high enough temperatures ($T \geq 160$ °C) in the case of the PS8 matrix, the CdS−S2VPs exhibit diffusive behavior. At low temperatures ($T \leq 130$ °C), however, their dynamics exhibit a crossover to hyper-diffusive dynamics. For the PS34 matrix, the CdS−S2VP dynamics are hyper-diffusive mode through entire temperature range studied (120 °C $\leq T \leq$ 180 °C).

EXPERIMENTAL SECTION

Poly(styrene-*b*-2 vinylpyridine) diblock copolymer was purchased from Polymer Source (Montreal, Quebec, Canada). The weight-averaged molecular weights of polystyrene and 2 vinylpyridine blocks were 44 and 8.4 kg/mol, respectively. We refer to this polymer as S2VP(44−8). Samples of PS homopolymer with the weight-averaged molecular weights of 8 (PS8) and 34.3 (PS34) kg/mol were also purchased from Polymer Source. Glass transition temperature of PS is ∼100 °C.[58] Critical entanglement molecular weight of PS is ∼32000 kg/mol.[59,60] Cadmium acetate dihydrate ($Cd(CH_3COO)_2{\cdot}sH_2O$), toluene, and methanol (MeOH) were purchased from Sigma-Aldrich (St. Louis, MO). Sodium sulfide anhydrous (Na_2S) was purchased from Alfa Aesar (Ward Hill, MA). No further purification was applied to these chemicals.

In order to synthesize CdS−S2VP, we followed a similar procedure as Koh et al.[24] First, S2VP micelles were formed by solvating them in toluene. Then, aqueous solutions of Cd^{2+} ion and Na_2S were sequentially added into the S2VP micelle suspension in toluene followed by vigorous stirring for over 24 h. The individual molar ratio of Cd^{2+} and Na^{2-} per pyridine ring is approximately 0.8. We then centrifuge the mixture for 10 min at 5000 rpm. The color of the centrifuged solution was transparent yellow. To incorporate the CdS−S2VPs in the PS matrices, 0.1 g of PS8 or PS34 was solvated in 10 mL of toluene. After preparing homopolymer solution, 10 mL of PS8 or PS34 solution was mixed with 20 mL of the CdS−S2VP suspension in toluene followed by vigorous stirring for more than 48 h. Detailed synthesizing procedure is provided by the Supporting Information.

The size of the individual CdS−S2VP was investigated by transmission electron microscopy (TEM) and DLS. For the TEM study, the CdS−S2VP suspension in toluene was drop-cast onto a carbon-coated TEM grid and dried at room temperature. Images were acquired by FEI Tecnai TF20 FEG 200 kV TEM (Hillsboro, OR). DLS was performed at the Advanced Photon Source (APS) in Argonne National Laboratory (ANL). The CdS−S2VP suspension in toluene was filled in a glass capillary tube (Charles Supper Company, Natick, MA). The capillary tube was then sealed and stored in the sample chamber. Measurements were performed with a custom-made DLS device with 633 nm wavelength light source at room temperature. The range of the scattering angle was varied from 15 to 150°. Surface force microscopy (SFM) analysis was performed by Bruker Multimode Atomic Force Microscopy (Digital Instruments, Santa Barbara, CA) with NSC15 Berkovich tip (MikroMasch, Lady's Island SC). The planar film was spun to 4 in. diameter polished silicon wafer for each of the samples: a neat CdS−S2VP solution, a mixture of CdS−S2VP and PS8 solution, and a mixture of CdS−S2VP and PS34 solution. The spun films were dried at room temperature. The dried films were then annealed at 120 °C in a vacuum oven for 12 h, followed by 30 min of solvent annealing in toluene atmosphere. The weight fraction of CdS from CdS−S2VP within PS homopolymer matrices was characterized by a thermal gravimetric analyzer (TGA) (TA Instruments, New Castle, DE). The average weight ratio was 3.42 ± 0.24% from both PS8 and PS34 matrices and the corresponding volume ratio is 0.68 ± 0.04%.

XPCS experiments were performed at beamline 8-ID-I at the APS at ANL. The photon energy was 7.35 keV, corresponding to a wavelength λ = 1.69 Å. Details regarding the beamline optics have been presented elsewhere.[44] Our measurements covered the wavevector range of $0.0038 < q < 0.028$ Å^{-1}. For these experiments, mixtures of CdS−S2VP with PS8 and mixtures of CdS−S2VP with PS34 are cured in the vacuum oven at 60 °C with continuous stirring. CdS−S2VP within the PS matrices was mounted in a sample holder comprised of a 1 mm-thick aluminum plate, penetrated by 1 mm diameter holes. The sample holder was thoroughly cleaned with ethanol (EtOH) and Milli Q water prior to use. To load the polymer sample, the sample holder was placed on a hot plate and heated to 120 °C. Then, the cured CdS−S2VP within PS matrices was placed so that it melted into the appropriate hole in the sample holder. Subsequently, the sample was annealed at 120 °C for 12 h and mounted in the experimental vacuum cell. The sample was then heated to 180 °C. We set an initial idling time of 60 min followed by measurements at 180 °C. Then, we cooled down the sample to next target temperature at 1 °C/min. At each target temperature, we set 60 min of idling time to stabilize the temperature before initiating data acquisition. By standardizing the temperature schedule in this manner, each sample experienced an identical thermal history. Thus, effects from aging should, in principle, be identical across all samples. The cross section of the X-ray beam was 20 μm × 20 μm. Each sample was divided into an imaginary grid with grid size of 40 μm × 40 μm. At each temperature, the scattering from 3 individual grid locations were measured for low and high q. A charge-coupled device (CCD) area detector captured 60 frames per second.[44] The average intensity as a

dx.doi.org/10.1021/ma500956b | Macromolecules XXXX, XXX, XXX−XXX

function of wavevector (i.e., SAXS intensity) and the intensity time autocorrelation function were obtained using 8-ID's XPCSGUI software.[61]

RESULTS AND DISCUSSION

The particle size of CdS−S2VP in toluene was measured with DLS and drop-cast TEM. Both approaches yielding an average diameter of ∼60 nm. Figure 1a shows a representative drop-cast TEM image of CdS−S2VP. The relatively dark spots observed can be attributed to individual CdS NPs with a size ranging around 5−6 nm, which is in good agreement with previously reported values.[24] Parts b−d of Figure 1 show tapping mode phase image of neat CdS−S2VPs, CdS−S2VPs in PS8 matrix, and CdS−S2VPs in PS34 matrix on silicon wafer, respectively. The area of scanned surface is 25 μm^2. The data scale range of neat CdS−S2VP and CdS−S2VP in PS matrices are 0−60° and 0−30°, respectively. The presented phase images display distinct circular buds which we ascribe to CdS−S2VPs. The higher data scale range of neat CdS−S2VP can be attributed to a stronger phase signal of CdS−S2VP buds which protrude due to the absence of a polymer matrix, Figure 1b. CdS−S2VPs in PS matrices, on the other hand, display circular buds with a less pronounced phase signal, Figure 1, parts c and d. The incorporation of the PS shells of CdS−S2VP with the PS matrix results in broadening of bud size. In particular, CdS−S2VP in PS8 matrix yields smaller bud sizes relative to PS34 matrix, which we attribute to the chain length difference of the PS matrices.

The coherent scattering intensity was measured over the wavevector range $0.0038 < q < 0.028$ Å^{-1}, which corresponds to 20−170 nm. The static intensity profiles are shown in the Supporting Information. The representative g_2s obtained for $q = 0.02103$ Å^{-1}, which corresponds to the length scale about the radius of CdS−S2VP, at various temperatures for PS8 and PS34 matrices is shown in Figure 2, parts a and b, respectively. Each experimentally measured g_2s exhibits a relaxation and converges to the unity with increasing delay time. We found eq 2, with fitting variables, A, β, and τ, sufficiently describes the observed g_2s for PS8 and PS34 matrices (shown as solid curves in Figure 2). The best fits of As are 0.4133 ± 0.0502 and 0.3719 ± 0.0357 for PS8 matrix and PS34 matrix, respectively.

Parts a and b of Figure 2 clearly illustrate that the observed dynamics slow markedly with decreasing temperature, irrespective of the matrix, which is characteristic of an increasing viscosity with decreasing temperature for both PS8 and PS34 matrix. On the other hand, aging may contribute to the protracted relaxation time trends that we have observed. Since PS8 and PS34 matrices underwent the same temperature schedule, both samples necessarily are subjected to the same aging condition at each measurement. Hence, although we do not measure the contributions of aging between measurements at different temperatures, the relative difference in the relaxation time between PS8 and PS34 matrices can be understood solely as a consequence of viscosity, albeit with the assumption that the dynamics of CdS−S2VP in the PS8 and PS34 matrices follow similar rates of aging. Evidently, for every given temperature, CdS−S2VP in PS8 matrix follows a faster relaxation process compared to CdS−S2VP in PS34 matrix. This implies that the condition within the PS8 matrix is less viscous than the PS34 matrix for a given temperature. This is certainly reasonable as PS8 has a smaller molecular weight relative to PS34.

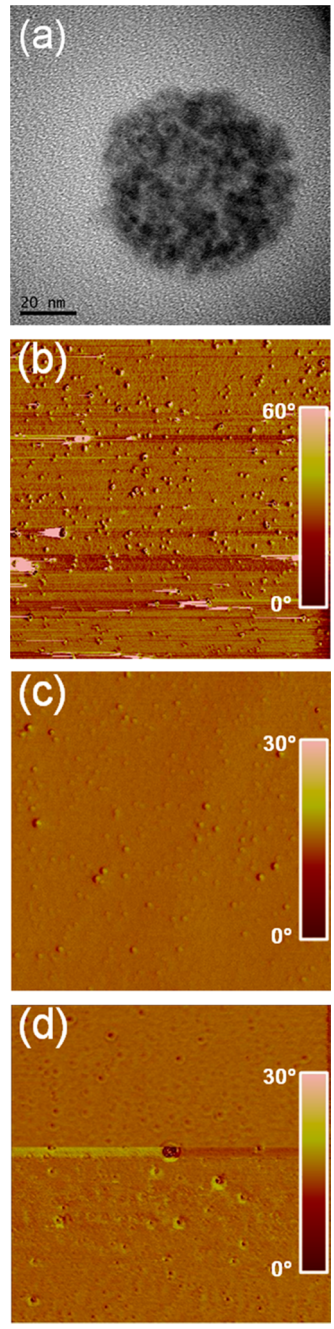

Figure 1. (a) Drop-cast TEM image of CdS−S2VP. We found good agreement from DLS and TEM. Both approaches yielding an average diameter of ∼60 nm. Tapping mode phase image of (b) neat CdS−S2VPs, (c) CdS−S2VPs in PS8, and (d) CdS−S2VPs in PS34. The scanned surface area for parts b−d is 25 μm^2. The data scale range for part b is 0−60° and the data scale range for parts c and d are 0−30°. The higher data scale range of neat CdS−S2VP (b) can be attributed to a stronger phase signal of CdS−S2VP buds which protrude due to the absence of a polymer matrix. The incorporation of the PS shells of CdS−S2VP with the PS matrix results in broadening of bud size. In particular, CdS−S2VP in PS8 matrix (c) yields a smaller bud sizes relative to PS34 matrix (d), which we attribute to the chain length difference of the PS matrices.

To explore the temperature dependence of the decay patterns, we use the logarithmic ISF

$$\ln[(g_1)^2] = -2(t_d/\tau)^{\beta} \quad (3)$$

dx.doi.org/10.1021/ma500956b | Macromolecules XXXX, XXX, XXX−XXX

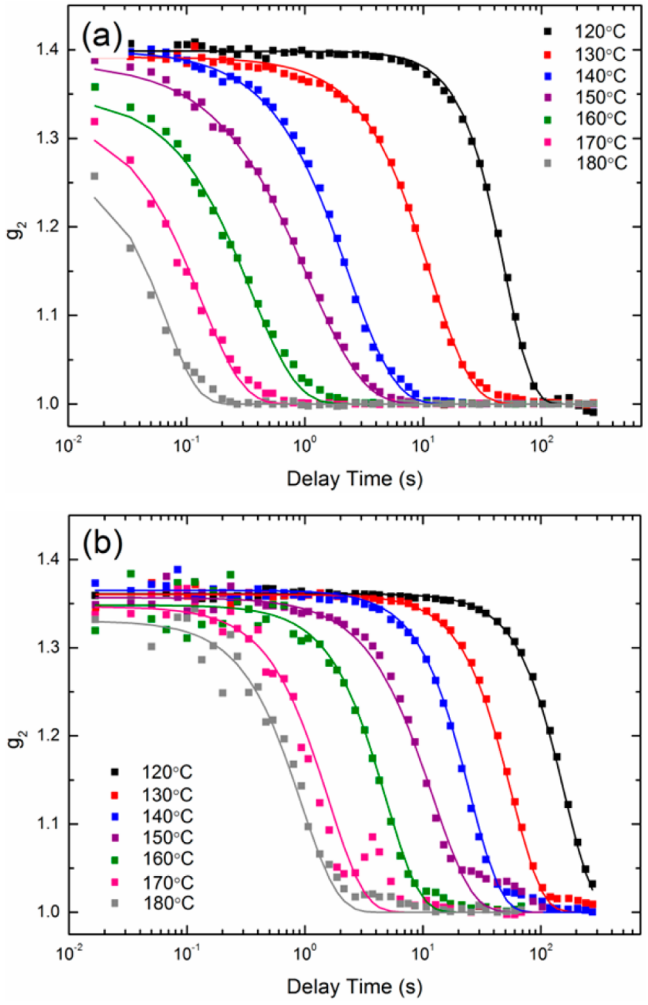

Figure 2. Representative g_2s from CdS−S2VP in (a) PS8 and (b) PS34 matrices obtained for q = 0.02103 Å^{-1} with various temperature. The solid squares and lines represent the experimental data and best fits, respectively, according to eq 2. For every given temperature, CdS−S2VP in PS8 matrix follows a faster relaxation process compared to CdS−S2VP in PS34 matrix.

where t_d/τ is reduced delay time and $\ln(g_1^2) = \ln((g_2 - 1)/A)$. The logarithmic ISFs versus linear reduced delay time implies that simple ($\beta = 1$), compressed ($\beta > 1$), and stretched ($0 < \beta < 1$) exponentials would appear as straight, negative, and positive curvature, respectively. Parts a and b of Figure 3 display the logarithmic ISF versus reduced delay time for CdS−S2VP in the PS8 matrix and PS34 matrix, respectively. Figure 3a illustrates that the logarithmic ISFs for CdS−S2VP in the PS8 matrix exhibits a change in curvature with decreasing temperature, which indicates a crossover in the observed dynamics. In particular, the logarithmic ISFs at 160−180 °C follow a relatively straight line corresponding to simple exponential decay, while the logarithmic ISF at 120 °C displays an apparent negative curvature (black curve) indicating compressed exponential relaxation. On the other hand, the logarithmic ISFs from PS34 matrix, shown in Figure 3b, exhibits negative curvatures, representing a compressed exponential relaxation, irrespective of the temperature. These trends are demonstrated more clearly by plotting the averaged βs over the wavevectors as a function of temperature in Figure 3c. For PS8 matrix, β monotonically decreases with increasing

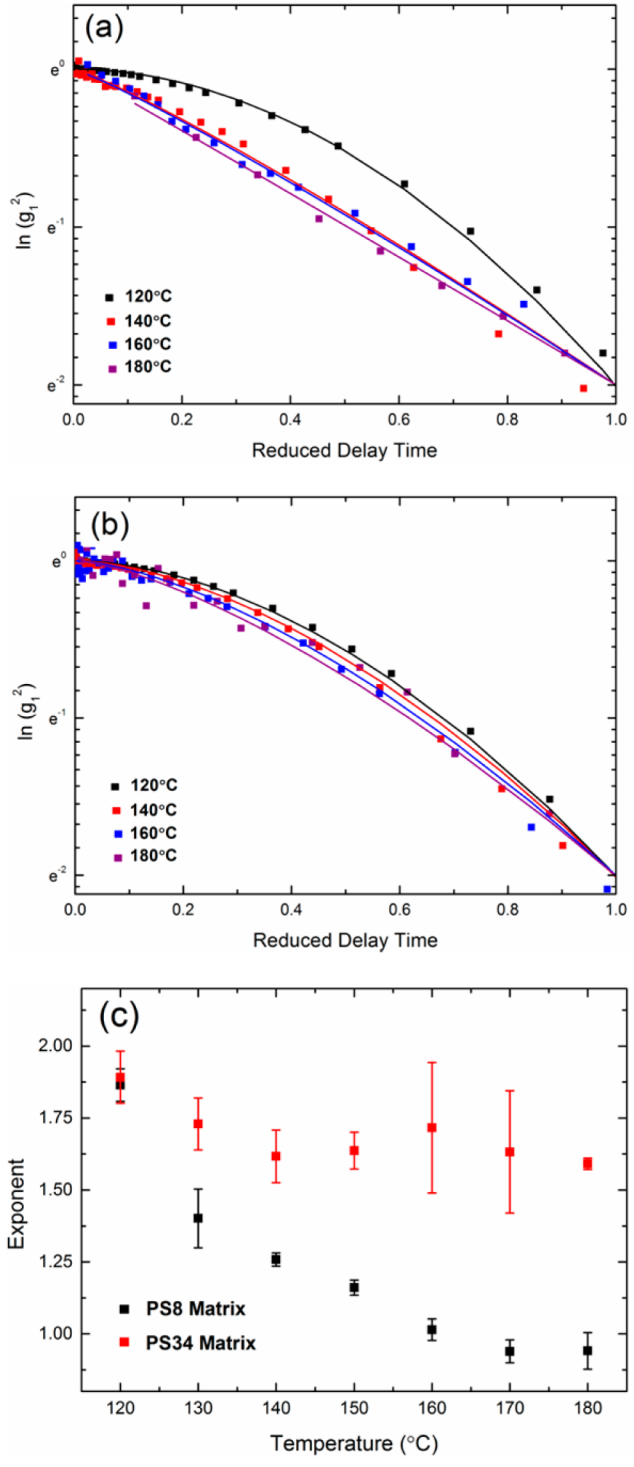

Figure 3. (a) Logarithmic ISF versus reduced delay time of CdS−S2VP in PS8 matrix at 0.02103 Å^{-1}. At 160 and 180 °C, the presented curves show straight or weak positive curvature corresponding to simple or stretched exponential decay, respectively, while the presented curve at 120 °C displays a negative curvature indicating compressed exponential relaxation. (b) Logarithmic ISF versus reduced delay time of CdS−S2VP in PS34 matrix at 0.02103 Å^{-1}.The presented curves from CdS−S2VP in PS34 matrix exhibit negative curvature at all temperatures studied indicating compressed exponential decay. (c) Averaged βs over the previously mentioned wavevector space.

dx.doi.org/10.1021/ma500956b | *Macromolecules* XXXX, XXX, XXX−XXX

temperatures from 120 to 160 °C reaching a plateau at $\beta \sim 1$ from 160 to 180 °C. The PS34 matrix, on the other hand, exhibit $\beta \geq 1.5$ throughout the temperatures studied.

The observed dynamics for PS8 matrix exhibits a crossover from simple to compressed exponential decay patterns corresponding to diffusive to hyper-diffusive dynamics with decreasing temperature, respectively. Crossover behavior from diffusive to hyper-diffusive dynamics have been observed from a variety of highly structured but disordered soft matter.[45−47,49,51−55] Even though the aforementioned CTRW can explain particle dynamics at all temperatures, we find the dynamics of CdS−S2VP in PS8 matrix are more consistent with SFR, which accommodates temperature dependent crossover behavior. In SFR, the underlying mechanism for crossover and hyper-diffusive dynamics has been explained on the basis of the elastic relaxation of heterogeneous local stresses.[47,50,57] At a relatively high temperature, CdS−S2VPs behave like non-interacting Brownian NPs. At lower relative temperatures, local strain fields resulting from the elastic relaxation of heterogeneous internal stresses bring about hyper-diffusive dynamics of CdS−S2VP matrices. By contrast, hyper-diffusive dynamics within PS34 matrix is exhibited irrespective of the temperatures explored. Cipelletti et al. pointed out that an overdamped matrix results in the hyper-diffusive dynamics of concentrated emulsions and surfactant system.[47] We hypothesize that the higher viscosity, resulting from the higher molecular weight of PS34 matrix may create such overdamped matrix conditions for the CdS−S2VPs. Thus, the observed dynamics would appear hyper-diffusive until a critical temperature was applied, which would sufficiently lower the viscosity and initiate a similar crossover behavior as found in the PS8 matrix.

The intensity correlation function, $g_1(\vec{R},t_d)$, for a Brownian particle given by a position vector $\vec{R}$ is a solution of the diffusion equation: $(\partial/\partial t_d)g_1(\vec{R},t_d) = D\cdot\nabla^2 g_1(\vec{R},t_d)$ where D is diffusivity.[62] Thus, it follows that the Fourier transformed intensity correlation function, $g_1(q,t_d)$, is also a solution of the Fourier transformed diffusion equation: $(\partial/\partial t_d)g_1(q,t_d) = -q^2 D\cdot g_1(q,t_d)$. The ISF for Brownian particles is a simple exponential decaying function.[62]

$$g_1(q, t_d) = \exp[-(q^2 D t_d)] = \exp[-(t_d/\tau)^{\beta=1}] \quad (4)$$

From eq 4, the characteristic relaxation time is given by $\tau = 1/(Dq^2)$. The theoretical slope of the logarithmic τ versus wavevector curves is −2. By contrast, experimental[45−47,49,51−55] and theoretical[47,57] investigation have revealed that the ISF for hyper-diffusive dynamics are given by

$$g_1 = \exp[-(t_d/\tau)^{\beta=1.5}] = \exp[-(\alpha q t_d)^{\beta=1.5}] \quad (5)$$

where α is a characteristic velocity, which will be discussed later. Consequently, τ is inversely proportional to the wavevector and the slope of logarithmic τ versus wavevector for hyper-diffusive dynamics is −1.

$$\tau = 1/(\alpha q) \quad (6)$$

Hence, the diffusion properties of CdS−S2VP in PS8 and PS34 matrices at various temperatures can be revealed by monitoring the slopes of the experimental ISF, of which, normal diffusion would yield a slope of −2 while hyper-diffusion would yield a slope of −1.

Parts a and b of Figure 4 show the wavevector dependence of τ at various temperatures for PS8 and PS34 matrices, respectively. Since the detector is limited to acquire a finite

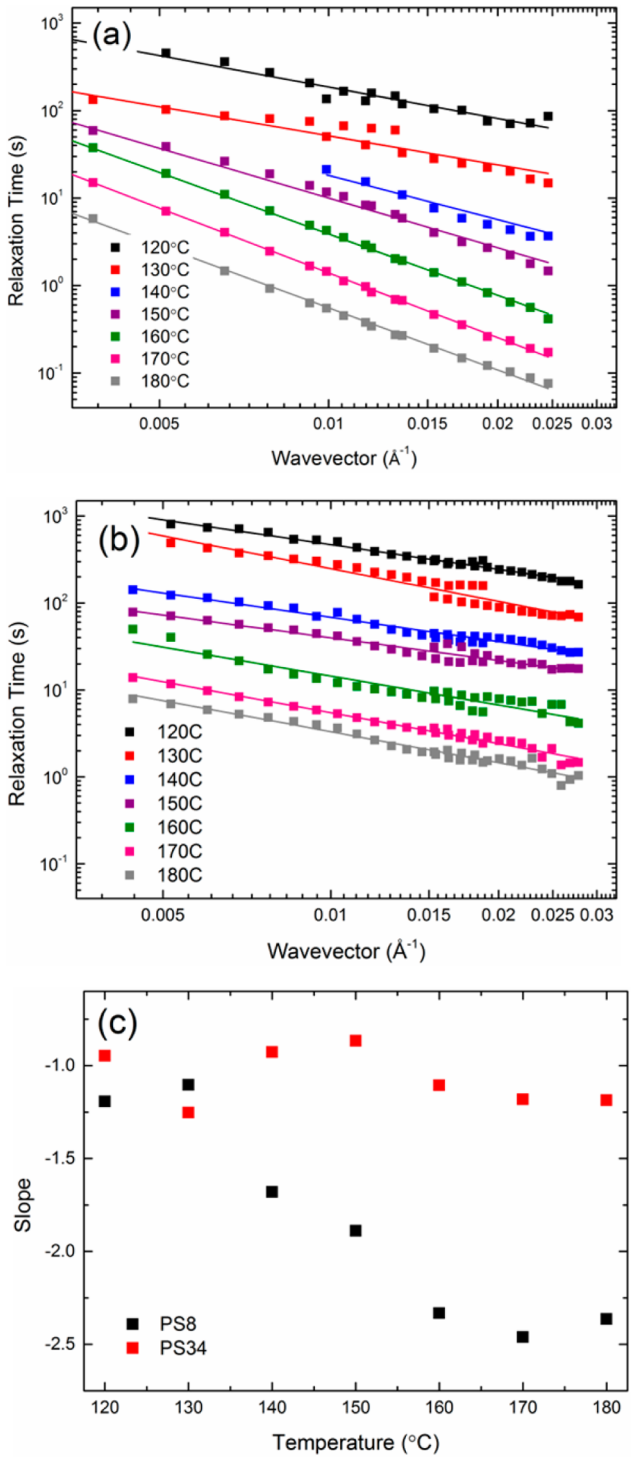

Figure 4. (a) Wavevector dependence of τ at various temperatures from CdS−S2VP in PS8 matrix. We observe a diffusive dynamics at 160, 170, and 180 °C. The average slope of logarithmic τ versus wavevector curves is −2.39 ± 0.07. On the other hand, relatively low and near the glass transition temperature of PS, T = 120 and 130 °C, τ versus wavevector curves exhibit hyper-diffusive dynamics with slope of −1.15 ± 0.06. (b) Wavevector dependence of τ at various temperatures from CdS−S2VP in PS34 matrix. The average slope of logarithmic τ versus wavevector curves from PS34 is −1.07 ± 0.15, indicating hyper-diffusive dynamics at all temperature studied, 120 °C ≤ T ≤ 180 °C. (c) Slope of logarithmic τ versus wavevector curves versus temperature.

dx.doi.org/10.1021/ma500956b | Macromolecules XXXX, XXX, XXX−XXX

space of wavevectors, we selected two different detection positions to build up the experimental wavevector space with an overlapping range between $0.015 < q < 0.018$ Å^{-1} to ensure a connectivity between the different sets of measurements. The age difference between low and high wavevector space, however, is inevitably observed in Figure 4b at 130, 150, 160, 170, and 180 °C. Figure 4a illustrates that the slopes of the τ versus wavevector curve change with temperature. Evidently, the slopes of the τ versus wavevector curves at different temperature indeed exhibit greater variability for PS8 matrix (Figure 4a) as compared to PS34 matrix (Figure 4b). The variation in the slopes for PS8 (black squares) and PS34 (red squares) is quantified in Figure 4c. Strikingly, the PS8 matrix exhibits three distinctive temperature regimes: diffusive dynamics (160−180 °C), transition range (140−150 °C), and hyper-diffusive dynamics (120−130 °C). In particular, the average slopes at 160, 170, and 180 °C is 2.39 ± 0.07 and β is 0.98 ± 0.07. These results suggests the PS8 matrix offers a diffusive condition for CdS−S2VPs for the temperature ranges of 160−180 °C. Deviations from diffusive dynamics begin to manifest at 140 and 150 °C followed by a strong indication of hyper-diffusive dynamics at 120 and 130 °C, which has a slope given by -1.15 ± 0.06 and $\beta = 1.65 \pm 0.28$. On the other hand, PS34 matrix creates a hyper-diffusive environment for CdS−S2VPs with minimal variability between the temperatures in this study. The slope of the PS34 matrix was found to be -1.07 ± 0.15.

From eq 6, the profiles of τ^{-1} versus q at each temperature (provided in the Supporting Information) are expected to show a linear relationship for hyper-diffusive dynamics; i.e., $\tau^{-1} = \alpha q$, where α represents the characteristic velocity. Evidently, Figure 5a shows α increases with temperature for CdS−S2VP in PS34 matrix. Because α is a temperature dependent rate property, we can characterize this relationship using the Arhenius equation which is given by $\alpha = \alpha_\infty \exp[(-E_a)/(k_B T)]$ where E_a is activation energy, T is temperature, k_B is Boltzmann constant, and $\alpha_\infty = \lim_{T\to\infty}\alpha$.[55] A black solid line in Figure 5a represents the best fits with $E_a = 2.138 \times 10^{-19}$ J and $\alpha_\infty = 2.408 \times 10^{16}$ Å/s.

In the SFR model, the particles and surrounding polymer are co-moving, so the particles should not experience a drag force. However, we assume that α is the average drift velocity inferred from XPCS measurements. To determine the force acting on CdS−S2VP, we adopt Stokes drag force which is given by

$$F = 6\pi\mu R_H \alpha \tag{7}$$

where μ is dynamic viscosity. Zero shear viscosity (η_0) substitutes for μ because α is less than 33 Å/s. The macroscopic viscosity of PS matrices was measured with a ARES-LS1 viscometer. Specifically, PS homopolymers were subjected to dynamic frequency sweep from 0.1 to 100 rad/s. The resultant macroscopic viscosity at each temperature is provided by Supporting Information. Remarkably, the values of the Stoke's drag force acting on CdS−S2VP from eq 7 decreases with increasing temperature. This observation confirms that the detected dynamics in the PS34 matrix would appear hyper-diffusive until a critical temperature was applied, which would correspondingly lower the force sufficiently and initiate a similar crossover behavior as found in the PS8 matrix. However, the values of the force in Figure 5b should not be interpreted within the context of the SFR model.

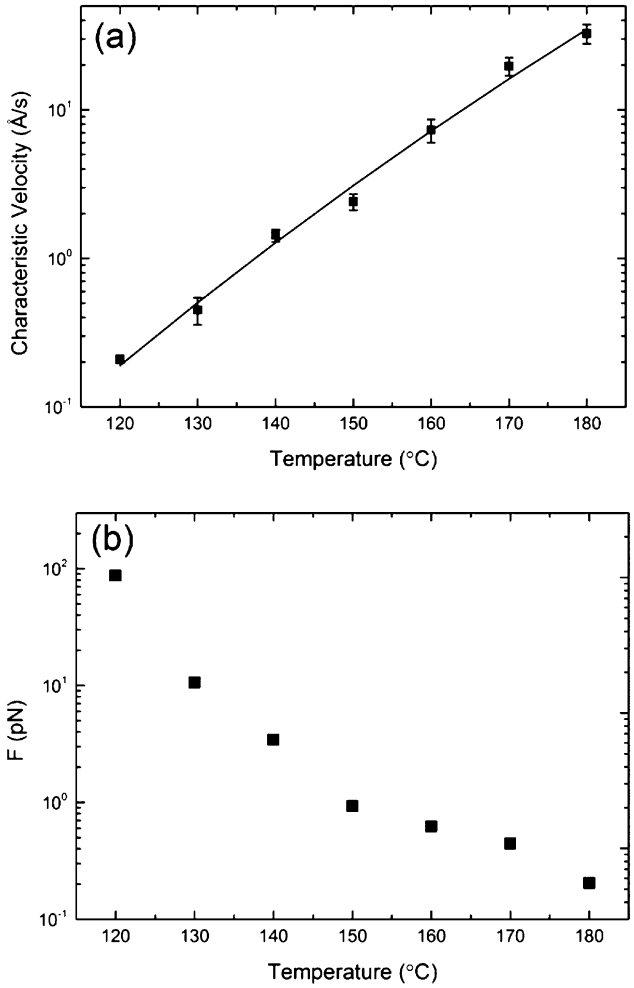

Figure 5. (a) Characteristic velocity, α, increases with increasing temperature. Because α is temperature dependent rate property, we describe the α versus temperature relationship using the Arhenius equation which is given by $\alpha = \alpha_\infty \exp[(-E_a)/(k_B T)]$. A black solid line represents the best fits with $E_a = 2.138 \times 10^{-19}$ J and $\alpha_\infty = 2.408 \times 10^{16}$ Å/s. (b) Stoke's drag force acting on CdS−S2VP decreases with increasing temperature.

CONCLUSIONS

We have successfully synthesized semiconductor NPs using solvent selective micellar diblock copolymer and investigated the crossover dynamics of the resulting CdS−S2VP in low and intermediate molecular weights, which is slightly higher than the critical entanglement molecular weight, polystyrene matrices with various temperatures: 120 °C $\leq T \leq$ 180 °C. For PS8 matrix, we observed the crossover behavior is well-represented as deviation of the ISF from simple to compressed exponential decay with decreasing temperature. On the other hand, CdS−S2VP in PS34 matrix exhibits hyper-diffusive dynamics and a compressed exponential decay at all temperatures studied. In addition, we found the logarithmic ISF versus linear reduced delay time and τ versus wavevector curves successfully reflect crossover and corresponding hyper-diffusive dynamics. When a simple or stretched exponential decay is found, CdS−S2VPs undergo diffusive dynamics. By contrast, compressed exponential decay is a signature of hyper-diffusive dynamics resulting from local strain field from SFR model.[47,57] Cipellitti et al. pointed out that the hyper-diffusive dynamics depend only on the characteristic velocity ($\alpha = qt_d$) rather than

dx.doi.org/10.1021/ma500956b | Macromolecules XXXX, XXX, XXX−XXX

on q and t_d separately.[47] Using this result, we determined a, the corresponding activation energy, and the typical force acting on the particles. Since, α can vary with aging time, samples at each temperature must have the same aging time to acquire an accurate activation energy. However, in the presented study, the aging time at each temperature is significantly different. Thus, the current activation energy should be treated as a rough estimation. Further investigation with identical aging time is required to decouple the viscosity and aging effects.

■ ASSOCIATED CONTENT

Ⓢ Supporting Information

Cadmium sulfide nanoparticles synthesizing procedure, static intensity profiles, profiles of τ^{-1} versus q, and frequency sweep rheology experiments and zero shear viscosity. This material is available free of charge via the Internet at http://pubs.acs.org.

■ AUTHOR INFORMATION

Corresponding Authors

*(W.-S.J.) E-mail: jangw@seas.upenn.edu and jangw428@gmail.com. Telephone: 979-574-5245.

*(S.G.M.) E-mail: simon.mochrie@yale.edu. Telephone: 203-436-4809. Fax: 203-432-6175.

Present Address

⊥Department of Chemical and Biomolecular Engineering, University of Pennsylvania, 220 South 33rd Street, 107 Towne Building, Philadelphia, PA 19104-6391

Notes

The authors declare no competing financial interest.

■ ACKNOWLEDGMENTS

This work was supported by the DOE Division of Basic Energy Sciences under Grant DE-SC0004162. Use of the Advanced Photon Source, an Office of Science User Facility operated for the U.S. Department of Energy (DOE) Office of Science by Argonne National Laboratory, was supported by the U.S. DOE under Contract No. DE-AC02- 06CH11357. The authors thank Thomas P. Russell for TGA experiments. We especially indebted to Chinedum Osuji and Xiaojun Di for frequency sweep rheology experiments.

■ REFERENCES

(1) Jang, W.-S.; Rawson, I.; Grunlan, J. C. *Thin Solid Films* **2008**, *516* (15), 4819−4825.

(2) Yin, S.-N.; Wang, C.-F.; Yu, Z.-Y.; Wang, J.; Liu, S.-S.; Chen, S. *Adv. Mater.* **2011**, *23* (26), 2915−+.

(3) Granstrom, M.; Berggren, M.; Inganas, O. *Science* **1995**, *267* (5203), 1479−1481.

(4) Coates, N. E.; Yee, S. K.; McCulloch, B.; See, K. C.; Majumdar, A.; Segalman, R. A.; Urban, J. J. *Adv. Mater.* **2013**, *25* (11), 1629−1633.

(5) Shenhar, R.; Norsten, T. B.; Rotello, V. M. *Adv. Mater.* **2005**, *17* (6), 657−669.

(6) Ulrich, R.; Zwanziger, J. W.; De Paul, S. M.; Reiche, A.; Leuninger, H.; Spiess, H. W.; Wiesner, U. *Adv. Mater.* **2002**, *14* (16), 1134−1137.

(7) Zhao, L.; Lin, Z. *Adv. Mater.* **2012**, *24* (32), 4353−4368.

(8) Mendes, L. C.; Silva, D. F.; Lino, A. S. *J. Nanosci. Nanotechnol.* **2012**, *12* (12), 8867−8873.

(9) Mokari, T.; Rothenberg, E.; Popov, I.; Costi, R.; Banin, U. *Science* **2004**, *304* (5678), 1787−1790.

(10) Anthony, S. P.; Kim, J. K. *Chem. Commun.* **2008**, *10*, 1193−1195.

(11) Sankaran, V.; Cummins, C. C.; Schrock, R. R.; Cohen, R. E.; Silbey, R. J. *J. Am. Chem. Soc.* **1990**, *112* (19), 6858−6859.

(12) Lee, Y.-K.; Hong, S. M.; Kim, J. S.; Im, J. H.; Min, H. S.; Subramanyam, E.; Huh, K. M. *Macromol. Res.* **2007**, *15* (4), 330−336.

(13) Rmili, A.; Ouachtari, F.; Bouaoud, A.; Louardi, A.; Chtouki, T.; Elidrissi, B.; Erguig, H. *J. Alloy. Compd.* **2013**, *557*, 53−59.

(14) Kakati, J.; Datta, P. *J. Lumin.* **2013**, *138*, 25−31.

(15) Nakanishi, T.; Maeda, M.; Kawashima, A.; Kamiya, S.; Fushimi, K.; Fujita, K.; Tanaka, K.; Hasegawa, Y. *J. Alloy. Compd.* **2013**, *562*, 123−127.

(16) Liang, G. X.; Fan, P.; Zheng, Z. H.; Luo, J. T.; Zhang, D. P.; Chen, C. M.; Cao, P. J. *Appl. Surf. Sci.* **2013**, *273*, 491−495.

(17) Grover, R.; Srivastava, R.; Chauhan, G.; Kamalasanan, M. N.; Mehta, D. S. *EPL (Europhys. Lett.)* **2012**, *99* (1), 17003.

(18) Grover, R.; Srivastava, R.; Rana, O.; Srivastava, A. K.; Maurya, K. K.; Sood, K. N.; Mehta, D. S.; Kamalasanan, M. N. *J. Lumin.* **2012**, *132* (2), 330−336.

(19) Zhao, H. Y.; Douglas, E. P.; Harrison, B. S.; Schanze, K. S. *Langmuir* **2001**, *17* (26), 8428−8433.

(20) Zhao, H. Y.; Douglas, E. P. *Chem. Mater.* **2002**, *14* (3), 1418−1423.

(21) Mossmer, S.; Spatz, J. P.; M?ller, M.; Aberle, T.; Schmidt, J.; Burchard, W. *Macromolecules* **2000**, *33* (13), 4791−4798.

(22) Jaramillo, T. F.; Baeck, S. H.; Cuenya, B. R.; McFarland, E. W. *J. Am. Chem. Soc.* **2003**, *125* (24), 7148−7149.

(23) Antonietti, M.; Wenz, E.; Bronstein, L.; Seregina, M. *Adv. Mater.* **1995**, *7* (12), 1000−&.

(24) Koh, H.-D.; Changez, M.; Lee, J.-S. *Macromol. Rapid Commun.* **2010**, *31* (20), 1798−1804.

(25) Koh, H.-D.; Kang, N.-G.; Lee, J.-S. *Langmuir* **2007**, *23* (23), 11425−11429.

(26) Bayramoglu, G.; Yilmaz, M.; Arica, M. Y. *Biores. Technol.* **2010**, *101* (17), 6615−6621.

(27) Henglein, A. *Chem. Rev.* **1989**, *89* (8), 1861−1873.

(28) Steigerwald, M. L.; Brus, L. E. *Acc. Chem. Res.* **1990**, *23* (6), 183−188.

(29) Uchman, M.; Prochazka, K.; Gatsouli, K.; Pispas, S.; Spirkova, M. *Colloid Polym. Sci.* **2011**, *289* (9), 1045−1053.

(30) Moffitt, M.; McMahon, L.; Pessel, V.; Eisenberg, A. *Chem. Mater.* **1995**, *7* (6), 1185−1192.

(31) Herron, N.; Wang, Y.; Eckert, H. *J. Am. Chem. Soc.* **1990**, *112* (4), 1322−1326.

(32) Lianos, P.; Thomas, J. K. *Chem. Phys. Lett.* **1986**, *125* (3), 299−302.

(33) Chen, W.; Lin, Z. J.; Wang, Z. G.; Lin, L. Y. *Solid State Commun.* **1996**, *100* (2), 101−104.

(34) Kannaiyan, D.; Kim, E.; Won, N.; Kim, K. W.; Jang, Y. H.; Cha, M.-A.; Ryu, D. Y.; Kim, S.; Kim, D. H. *J. Mater. Chem.* **2010**, *20* (4), 677−682.

(35) Yabu, H.; Endo, A.; Koike, K.; Motoyoshi, K.; Higuchi, T.; Shimomura, M. *Polym. J.* **2011**, *43* (3), 301−305.

(36) Schaertl, W.; Roos, C. *Phys. Rev. E* **1999**, *60* (2), 2020−2028.

(37) Kroon, M.; Wegdam, G. H.; Sprik, R. *Phys. Rev. E* **1996**, *54* (6), 6541−6550.

(38) Ghofraniha, N.; Conti, C.; Ruocco, G.; Zamponi, F. *Phys. Rev. Lett.* **2009**, *102* (3), 038303.

(39) Maggi, C.; Di Leonardo, R.; Ruocco, G.; Dyre, J. C. *Phys. Rev. Lett.* **2012**, *109* (9), 097401.

(40) Carn, F.; Boue, F.; Djabourov, M.; Steunou, N.; Coradin, T.; Livage, J.; Floquet, S.; Cadot, E.; Buhler, E. *Soft Matter* **2012**, *8* (10), 2930−2944.

(41) Fall, A. B.; Lindstrom, S. B.; Sprakel, J.; Wagberg, L. *Soft Matter* **2013**, *9* (6), 1852−1863.

(42) Grossiord, N.; Loos, J.; van Laake, L.; Maugey, M.; Zakri, C.; Koning, C. E.; Hart, A. J. *Adv. Funct. Mater.* **2008**, *18* (20), 3226−3234.

(43) Sutton, M.; Mochrie, S. G. J.; Greytak, T.; Nagler, S. E.; Berman, L. E.; Held, G. A.; Stephenson, G. B. *Nature* **1991**, *352* (6336), 608−610.

(44) Falus, P.; Borthwick, M. A.; Mochrie, S. G. J. *Rev. Sci. Instrum.* **2004**, *75* (11), 4383−4400.
(45) Caronna, C.; Chushkin, Y.; Madsen, A.; Cupane, A. *Phys. Rev. Lett.* **2008**, *100* (5), 055702.
(46) Falus, P.; Borthwick, M. A.; Narayanan, S.; Sandy, A. R.; Mochrie, S. G. J. *Phys. Rev. Lett.* **2006**, *97* (6), 066102.
(47) Cipelletti, L.; Ramos, L.; Manley, S.; Pitard, E.; Weitz, D. A.; Pashkovski, E. E.; Johansson, M. *Faraday Discuss.* **2003**, *123*, 423−423.
(48) Duri, A.; Cipelletti, L. *Europhys. Lett.* **2006**, *76* (5), 972−978.
(49) Chung, B.; Ramakrishnan, S.; Bandyopadhyay, R.; Liang, D.; Zukoski, C. F.; Harden, J. L.; Leheny, R. L. *Phys. Rev. Lett.* **2006**, *96* (22), 228301−228301.
(50) Cipelletti, L.; Manley, S.; Ball, R. C.; Weitz, D. A. *Phys. Rev. Lett.* **2000**, *84* (10), 2275−2278.
(51) Bandyopadhyay, R.; Liang, D.; Yardimci, H.; Sessoms, D. A.; Borthwick, M. A.; Mochrie, S. G. J.; Harden, J. L.; Leheny, R. L. *Phys. Rev. Lett.* **2004**, *93* (22), 228302.
(52) Bellour, M.; Knaebel, A.; Harden, J. L.; Lequeux, F.; Munch, J. P. *Phys. Rev. E* **2003**, *67* (3), 031405.
(53) Parashchuk, O. D.; Laptinskaya, T. V.; Ananieva, M. S.; Paraschuk, D. Y. *Soft Matter* **2011**, *7* (12), 5585−5594.
(54) Guo, H.; Ramakrishnan, S.; Harden, J. L.; Leheny, R. L. *J. Chem. Phys.* **2011**, *135* (15), 154903−154903.
(55) Guo, H.; Bourret, G.; Corbierre, M. K.; Rucareanu, S.; Lennox, R. B.; Laaziri, K.; Piche, L.; Sutton, M.; Harden, J. L.; Leheny, R. L. *Phys. Rev. Lett.* **2009**, *102* (7), 075702.
(56) Bouchaud, J. P.; Georges, A. *Phys. Rep.—Rev. Sect. Phys. Lett.* **1990**, *195* (4−5), 127−293.
(57) Bouchaud, J. P.; Pitard, E. *Eur. Phys. J. E* **2001**, *6* (3), 231−236.
(58) Fox, T. G.; Flory, P. J. *J. Appl. Phys.* **1950**, *21* (6), 581−591.
(59) Ueno, H.; Otsuka, S.; Kishimoto, A. *Kobunshi Ronbunshu* **1978**, *35* (5), 339−344.
(60) Plazek, D. J.; Orourke, V. M. *J. Polym. Sci., Part A-2: Polym. Phys.* **1971**, *9* (2), 209−&.
(61) Lumma, D.; Lurio, L. B.; Mochrie, S. G. J.; Sutton, M. *Rev. Sci. Instrum.* **2000**, *71* (9), 3274−3289.
(62) Berne, B. J.; Pecora, R. *Dynamic Light Scattering*; Dover: Mineola, NY, 2000.

Macromolecules

Article

pubs.acs.org/Macromolecules

The Static and Dynamic Structure Factor of a Diblock Copolymer Melt via Small-Angle X-ray Scattering and X-ray Photon Correlation Spectroscopy

Woo-Sik Jang,[†] Peter Koo,[†] Marcin Sykorsky,[‡] Suresh Narayanan,[§] Alec Sandy,[§] and Simon G. J. Mochrie*,[†]

[†]Deparment of Physics, Yale University, New Haven, Connecticut 06511, United States

[‡]Linac Coherent Light Source, Stanford Linear Accelerator Laboratory, Menlo Park, California 94025, United States

[§]Advanced Photon Source, Argonne National Laboratory, Argonne, Illinois 60439, United States

ABSTRACT: We present a detailed X-ray scattering study of the static and dynamic behavior of a styrene−isoprene diblock copolymer melt with a styrene volume fraction of 0.3468. At 115 and 120 °C, we observe splitting of the principal Bragg peak, which we attribute to phase coexistence of hexagonal cylindrical and cubic double-gyroid structure. In the disordered phase, above 130 °C, we have characterized the dynamics of composition fluctuations via X-ray photon correlation spectroscopy. Near the peak of the static structure factor, these fluctuations show stretched-exponential relaxations, characterized by a stretching exponent of about 0.36 for a range of temperatures immediately above the MST. The corresponding characteristic relaxation times vary exponentially with temperature, changing by a factor of 2 for each 2 °C change in temperature. At low wavevectors, the measured relaxations are diffusive with relaxation times that change by a factor of 2 for each 8 °C change in temperature.

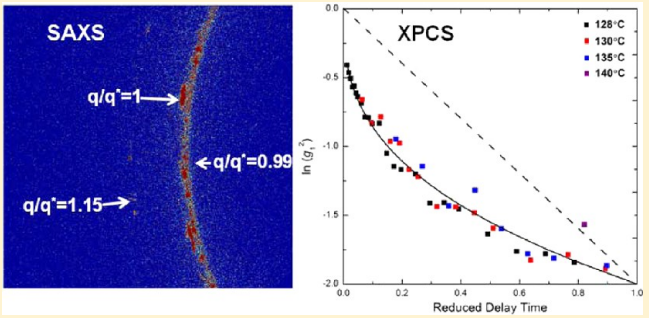

INTRODUCTION

Block copolymers (BCP) have attracted increasing attention for various applications, often as a result of their ability to self-assemble into nanostructures, periodic and otherwise. Applications of BCP that have already been realized include biomimetic filtration membranes,[1] selective gas separation systems,[2] solution separation membranes,[3] ion exchange membranes for fuel cells,[4] synthesizing nanoporous thin films,[5] and fabricating semiconductor nanostructures.[6] In spite of a tremendous amount of work on the phase behavior and static structures of BCPs, the structural dynamics of these materials are relatively little studied and poorly understood. In part, this is because BCP dynamics compound the difficulties of polymer dynamics with the complications caused by nanoscale inhomogeneities associated with differing block concentrations at different locations, sometimes with highly different individual diffusivities and viscosities. In addition, many of the key methods for elucidating structure are less successful for characterizing dynamic behavior.

Recently, Patel et al. studied the structural and stress relaxation time of highly asymmetric poly(styrene$_{7K}$-*b*-isoprene$_{27K}$) diblock copolymer, SI(7−27), using X-ray photon correlation spectroscopy (XPCS) to characterize the structural dynamics of this material.[7,8] Even the disordered phase of asymmetric diblocks, such as SI(7−27), show a strong segregation between blocks, and as a result they realize a disordered micelle phase near the micophase-separation transition (MST).[8] Therefore, the structural dynamics characterized by Patel et al. correspond to micelle diffusion. By contrast, at smaller asymmetries, there are no micelles in the disordered phase. We may therefore expect dynamics of a different character at smaller asymmetries. The goal of the present work was to characterize the dynamics of a block copolymer melt in the nonmicellar regime. Accordingly, we carried a careful synchrotron small-angle X-ray scattering (SAXS) and XPCS study of poly(styrene$_{10K}$-*b*-isoprene$_{16.5K}$), SI(10−16.5), with a polystyrene volume fraction of $f = 0.35$. In addition to the static and dynamic behavior near the peak of the scattering function at nonzero wavevectors, we also characterized the excess scattering that occurs at very small angles, via SAXS and XPCS. Although similar scattering is observed ubiquitously in polymer systems, its origin remains obscure. Here, we reveal this component of the scattering to be dynamic. Interestingly, the dynamics associated with the excessive scattering at small wavevectors show different temperature dependence to the dynamics near the peak of the scattering function.

Received: July 10, 2013
Revised: September 19, 2013
Published: October 30, 2013

   dx.doi.org/10.1021/ma4014548 | *Macromolecules* 2013, 46, 8628−8637

Ordered Phase Structures near $f = 0.35$. Some of the most intriguing BCP ordered structures are cubic or similar multiply connected morphologies. Such structures occur near $f = 0.35$ (close to the composition of the material studied here). Hajduk et al. performed SAXS and transmission electron microscopy (TEM) on poly(styrene-*b*-isoprene) (SI) and reported a cubic double-gyroid structure in weakly segregated SI melts.[9] Khandpur et al. used TEM to confirm the existence of the double-gyroid.[10] Beyond cubic phases, Epps et al. discovered an equilibrium orthorhombic *Fddd* structure in a poly(isoprene-*b*-styrene-*b*-ethylene oxide) (ISO) triblock copolymer.[11] The *Fddd* structure is built from similar structural elements to the double gyroid, but arranged differently, leading to the loss of cubic symmetry, although there is a near-coincidence of wavevectors for the first three orthorhombic scattering peaks—(004), (111), and (022)—which coincide for an orthorhombic unit cell with cell parameters (a, b, c) with ratios $(1{:}2{:}2\sqrt{3})$.[12−15]

Disordered-Phase Structure Factor Models. For the static scattering profile of disordered-phase BCPs, using only the volume fraction of one block, f, and the product of the molecular interaction parameter and the polymerization index, χN, Leibler's model predicts a structure factor of the form[16]

$$S_L = \frac{N}{F(x,f) - 2\chi N} \tag{1}$$

where $x = (qR_g)^2 = q^2(Nb^2)/6$, and the function, $F(x,f)$, is given by

$$F(x,f) = \frac{g_1(x,1)}{g_1(x,f)g_1(x,1-f) - [g_1(x,1) - g_1(x,f) - g_1(x,1-f)]^2/4} \tag{2}$$

where f is minor block volume fraction, and $g_1(x,f) = 2[fx - 1 + \exp(-fx)]/x^2$ is the Debye function. Equation 2 is independent of temperature and has a minimum at $x^* = (q_L{}^*R_g)^2$, where $q_L{}^*$ is the theoretical peak wavevector according to Leibler's model. Therefore, $q_L{}^*$ is also independent of temperature. When $2\chi N$ is equal to the minimum value, $F[x^* = (q_L{}^*R_g)^2, f]$, Leibler's structure factor, $S_L(q_L{}^*)$, diverges and a spinodal value, $(\chi N)_S$, can be calculated. For symmetric diblock copolymers, $(\chi N)_S = 10.495$ and $q^*R_g = 1.95$. Because SI(10−16.5) is asymmetric, the expected spinodal value is $(\chi N)_S = 12.67$.[17] While eq 1 has been found to be in reasonable agreement with experimental studies on diblock copolymers for relatively high temperature or heavy molecular weight, it appears to be less accurate in the vicinity of the MST. Subsequently, Leibler,[18] Hong et al.,[19] and Burger and Semenov[20] showed theoretically that polydispersity has a marked effect on the scattering curves of block copolymer melts.

In contrast to the predictions of eq 1, numerous experimental[7,21,22] and theoretical[23−28] studies have shown a variation of the disordered-phase peak position with varying temperatures. Bates and co-workers attributed this shift to an increasing deviation from ideal Gaussian chain statistics with increasing proximity to the transition to the ordered phase.[28,29] Wang et al. proposed theoretically that the peak shift is the result of a change in micelle volume fraction in a BCP with a micellar character.[30] Recently, however, Morse and co-workers established renormalized one-loop (ROL) theory, which more accurately accounts for the effect of composition fluctuations.[31−33] On this basis, they show that the normalized peak wavevector, $q^*/q_L{}^*$ varies with varying χN, even for weakly segregated BCPs.

Lin et al.[21] performed SANS and Abuzaina et al.[34] performed SAXS on various SI diblock copolymers in the disordered phase. Abuzaina et al. fitted the scattering intensity according to Leibler's model to reveal a linear relationship between χ and T^{-1}, namely

$$\chi = -0.0043 + 13.31T^{-1} \tag{3}$$

Abuzaina et al. proposed that the disordered phase in the SI system for a volume fraction $0.25 < f < 0.5$ exhibits such a linear relationship between χ and $1/T$, eq 3, regardless of N and f.

These models[16,17,20,29] can explain the observed scattering profiles of disordered-phase BCPs at intermediate wavevectors ($0.02 < q < 0.05$ Å^{-1}) near the peak at q^*. However, at low wavevectors ($q < 0.02$ Å^{-1}), they predict a relatively small scattering intensity. By contrast, a number of experimental scattering studies on BCP reveal unexpectedly large scattering intensities at low wavevectors.[35−38] Even in studies of polymer solutions, where the small-angle scattering is expected to be described by a Lorentzian, excess small-angle scattering is often reported.[39] Koberstein et al. attributed this excess scattering to long-range random heterogeneities, with correlation lengths several times the polymer radius of gyration. According to these authors, the experimental small-angle scattering intensity can be well described by the sum of a Lorentzian plus a Lorentzian-squared.

Disordered-Phase Dynamics. The dynamics of BCP melts and blends are complicated because their constituent polymer chains can be entangled and because of the different diffusion properties of each chemically different block. Reptation models of polymer dynamics[25,26] are the commonly accepted theory of molecular dynamics of large-molecular-weight melts and blends. Diblock copolymer dynamics have been studied using dielectric spectroscopy,[40] forced Rayleigh scattering,[41] and nuclear magnetic resonance spectroscopy.[42] In an important study, Semenov et al. focused on the relaxation modes of compositional fluctuations in disordered symmetric diblock copolymer solutions, both theoretically and experimentally.[43−46] They found that they could account for their light scattering measurements via a linear summation of reptation and Rouse relaxation modes.

Mochrie et al.[47] first applied XPCS to study the dynamic behavior of BCP nanostructures[48] to which the length scales accessible by XPCS (∼ 20 nm) are well matched. Other applications of XPCS to pure polymer systems include the dynamic behavior of capillary waves on silicon substrates,[49] the structural relaxations of a highly asymmetric SI(7−27) diblock copolymer,[7,8] and the dynamics of polymer bicontinuous microemulsions[50] and sponge phases.[51,52] Neutron spin echo gives access to polymer dynamics at relatively fast time scales, $\sim 10^{-7}$ s or less, and relatively large wavevectors.[53]

Patel et al. studied the dynamics of a highly asymmetric SI(7−27) diblock using rheology and XPCS.[7] Their XPCS measurements found exponential relaxations near the peak of the static structure factor, and were interpreted in terms of micelle diffusion, because the system studied was highly asymmetric. Patel et al.'s rheology measurements yielded terminal relaxation times (τ_T) that were 1−2 orders of magnitude faster than the structural relaxation times (τ) measured via XPCS. In addition, the temperature dependence of τ was observed to be somewhat weaker than that of τ_T.

dx.doi.org/10.1021/ma4014548 | *Macromolecules* 2013, 46, 8628−8637

Here, we present a comprehensive experimental study of the structure and dynamics of a less asymmetric SI diblock copolymer, SI(10−16.5), with a volume ratio (f = 0.35), which is not expected to realize micelles in the disordered phase. For temperatures below the order−disorder transition (ODT), which occurs near 128 °C, the ordered nanostructures were investigated using SAXS. In the disordered phase, the static structure factor was studied via SAXS, while XPCS experiments were performed to investigate the relaxation of disordered-phase compositional fluctuations.

EXPERIMENTAL SECTION

SI diblock copolymer was purchased from Polymer Source (Montreal, Quebec, Canada). The weight-averaged molecular weights of polystyrene and polyisoprene blocks were 10 and 16.5 kg/mol, respectively. We refer to this polymer as SI(10−16.5). The volume fraction of the polystyrene block is f = 0.3468. The polydispersity index (PDI) is 1.09. No further purification was applied. To verify the effects of thermal annealing, size exclusive chromatography (SEC) analysis was performed by private company (Polymer Source, Montreal Canada). SAXS and XPCS experiments were performed at beamline 8-ID-I at the Advanced Photon Source (APS) at Argonne National Laboratory. The photon energy was 7.35 keV, corresponding to a wavelength λ = 1.69 Å^{-1}. Our measurements covered the range of wavevectors 0.004 < q < 0.07 Å^{-1}. For these experiments, polymer samples were mounted in a sample holder, comprising a 1.5 mm thick aluminum plate penetrated by two 1 mm diameter holes—one to contain the sample and the other to permit measurements of the X-ray beam intensity without the sample. The sample holder was thoroughly cleaned with ethanol and Milli-Q water prior to use. To load the polymer sample, the sample holder was placed on the hot plate and heated to 120 °C. Then, the as-received SI(10−16.5) was placed so that it melted into the appropriate hole in the sample holder. Although the polymer melts, it does not flow out because of its viscosity and surface tension. The sample was then annealed in a vacuum oven at 120 °C for more than 12 h and then mounted in the experimental vacuum cell.

For the X-ray measurements, the sample was heated to 150 °C and subsequently cooled to the target temperature at 0.5 °C/min. At each temperature, we waited 15 min to stabilize the temperature before initiating data acquisition. The cross section of the X-ray beam was 30 μm × 30 μm. Each sample was divided into an imaginary grid with grid size 50 μm × 50 μm. At each temperature, the scattering from 30 individual grid locations was measured in order to minimize the X-ray exposure of any particular portion of the sample. A CCD area detector captured 60 frames/s.[51] A total of 5120 frames were acquired at each grid position in an aggregate exposure time of 85.33 s, which is longer than the measured relaxation time at all temperatures studied. The average intensity as a function of wavevector (i.e., the SAXS intensity) and the intensity time autocorrelation function were obtained using 8-ID's XPCSGUI software.[54]

RESULTS AND DISCUSSION

Ordered Phases. Figure 1 shows representative two-dimensional (2D) scattering patterns, obtained as CCD images, at temperatures of 115, 120, 125, and 130 °C. Figure 1a (115 °C) and Figure 1b (120 °C) exhibit two strong, textured rings, which correspond to Bragg peaks at q_g* (first from right) and q_c*(second from right), respectively. A number of Bragg peaks in a ring near q/q_g* ≅ $(4/3)^{1/2}$ may also be discerned in this figure. By 125 °C, Figure 1c shows a single Bragg peak, and by 130 °C, Figure 1d shows no sign of any Bragg peaks, indicating that at 130 °C the SI(10−16.5) is in the disordered phase. Hence, directly from these 2D images, we may deduce the occurrence of phase transitions of the SI(10−16.5) diblock copolymer with varying temperature.

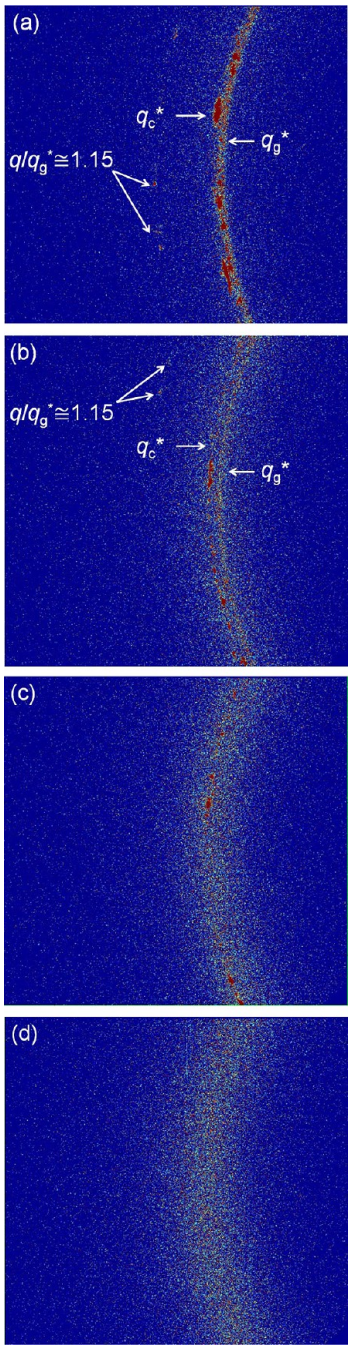

Figure 1. Representative CCD images at 115 (a), 120 (b), 125 (c), and 130 °C (d). (a) (115 °C) and (b) (120 °C) each show two strong, textured rings which correspond to Bragg peaks, emanating from multiple crystallites within the sample. (c) shows a single Bragg peak. (d) shows only diffuse scattering, indicating that at 130 °C SI(10−16.5) realizes a disordered phase.

In Figure 2, we present the azimuthally averaged SAXS profiles at various temperatures, also averaged over the 30 repeats at different grid positions. Strong Bragg peaks may be seen at 115, 120, and 125 °C. The first and second peaks from the left we identify as the principal peak of cubic double-gyroid and hexagonal cylindrical structure, respectively. A detailed explanation is presented below. The wavevector ratio of third peak from left at 115 and 120 °C is then q/q_g* ≅ $(4/3)^{1/2}$. These peaks, then, correspond to the rings of scattering, evident in Figures 1a and 1b. At 125 °C, the peaks at q_g* and q/q_g* ≅

dx.doi.org/10.1021/ma4014548 | Macromolecules 2013, 46, 8628−8637

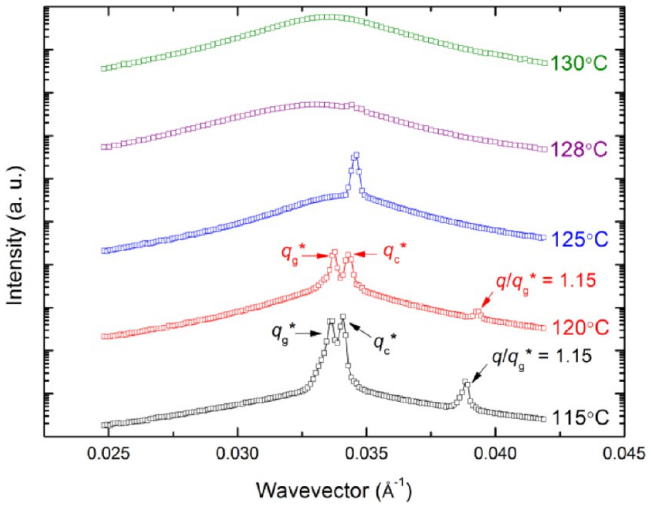

Figure 2. Azimuthally averaged SAXS profiles at 115, 120, 125, 128, and 130 °C for wavevectors between 0.025 and 0.042 Å^{-1}. The strong double peaks observed at 115 and 120 °C correspond to the two prominent, textured rings in Figures 1a and 1b, respectively. At 128 and 130 °C, the Bragg peaks from the ordered structures are replaced by disorder-phase scattering.

$(4/3)^{1/2}$ disappear, and a single Bragg peak remains in the profile. At 128 °C, the 30 repeats data set is composed of 14 measurements in which a Bragg peak may be discerned and 16 measurements in which none can be discerned. At 130 °C, only the single broad peak is observed at each grid position studied. Figures 1 and 2 indicate that the MST of the current SI(10–16.5) diblock copolymer is near 128 °C. Rheology is often used to identify the MST of block copolymers.[55−57] It is clear from these data that high-resolution synchrotron-based SAXS also provides an accurate method to determine the MST.

Coexistence of Different Morphologies. In Figure 3, we present the detailed evolution of SAXS intensity profiles with changes in temperature. The sample was heated to 150 °C and subsequently cooled to the target temperature. Thus, the sample experienced a phase transition from a disordered to an ordered state. The Bragg peaks in Figure 3a represent the initial ordered structure at 125 °C. The wavevector ratios between a main Bragg peak at q^* = 0.034 617 Å^{-1} and peaks at q = 0.059 941 and 0.069 134 Å^{-1} are 1.732 ($\sim\sqrt{3}$) and 1.997 ($\sim$2), respectively. These wavevector ratios suggest the existence of a hexagonal cylindrical structure.[58−60] The corresponding Miller indices for the hexagonal cylindrical structure peaks at q/q^* = 1, $\sqrt{3}$, and 2 are $(100)_c$, $(110)_c$, and $(200)_c$, respectively. After the measurements at 125 °C, the sample was cooled to 120 °C. Interestingly, the SAXS profile at 120 °C (Figure 3b) shows a splitting of the main peak, q^* = 0.033 764 and 0.034 297 Å^{-1}, and an appearance of peaks at q = 0.039 002, 0.059 417, and 0.068 939 Å^{-1}. The observation of two closely spaced peaks suggests that two different morphologies may coexist. After careful consideration of wavevector ratios, we ascribe this splitting to a coexistence of hexagonal cylindrical and cubic double-gyroid structure. In Figure 3b, the first peak from left is the principal peak of cubic double-gyroid structure, q_g^* = 0.033 764 Å^{-1}. The wavevector ratios between q_g^* and q = 0.039 002 and 0.068 939 Å^{-1} are $q/q_g^* \cong (4/3)^{1/2}$ and 2, respectively. A peak at $q/q_g^* \cong (4/3)^{1/2}$ is a signature of a cubic double-gyroid structure.[11,61−64] The corresponding Miller indices for the cubic double-gyroid structure peaks at q/q_g^* = 1, $(4/3)^{1/2}$, and

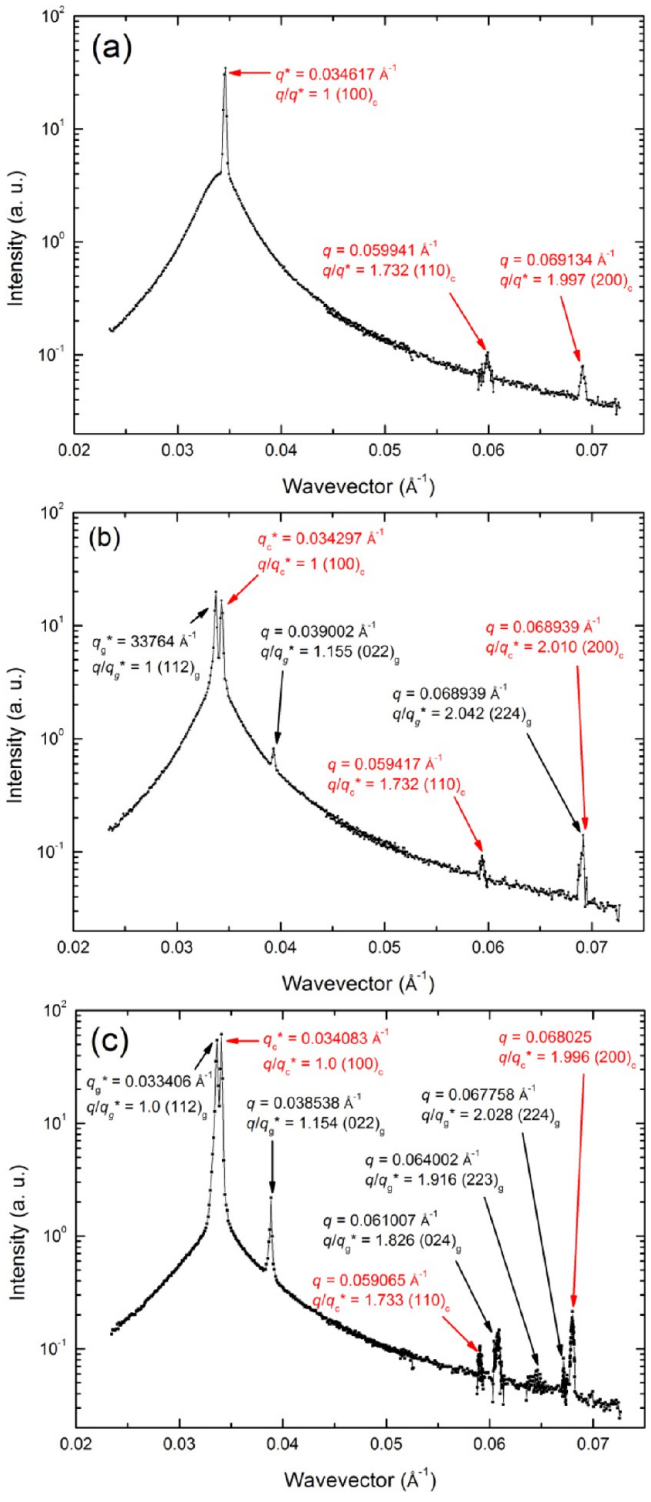

Figure 3. Azimuthally averaged SAXS profiles at (a) 125, (b) 120, and (c) 115 °C. In all SAXS profiles, peaks are indexed according to the cubic double-gyroid (black character and arrow) and hexagonal cylindrical (red character and arrow) structure groups.

2 are $(112)_g$, $(022)_g$, and $(224)_g$, respectively. The second peak from left is then identified as the main peak of hexagonal cylindrical structure, q_c^* = 0.034 297 Å^{-1}. The wavevector ratio between q_c^* and q = 0.059 417 and 0.068 939 Å^{-1} are $q/q_c^* \cong \sqrt{3}$ and 2, respectively. The corresponding Miller indices for the hexagonal cylindrical structure peaks at q/q^* = 1, $\sqrt{3}$, and 2 are $(100)_c$, $(110)_c$, and $(200)_c$, respectively. After the

dx.doi.org/10.1021/ma4014548 | Macromolecules 2013, 46, 8628−8637

measurements at 120 °C, the sample was cooled to 115 °C. Figure 3c exhibits the SAXS profile at 115 °C. The main peak is also observed to be split at 115 °C. Further, a series of peaks are observed. First and second peaks from left are regarded as q_g^* = 0.033 406 Å^{-1} and q_c^* = 0.034 083 Å^{-1}, respectively. The signatures of hexagonal cylindrical structure are observed at q = 0.059 065 Å^{-1} ($q/q_c^* \cong \sqrt{3}$) and q = 0.068 025 Å^{-1} ($q/q_c^* \cong 2$). The corresponding Miller indices for the hexagonal cylindrical structure peaks at q/q^* = 1, $\sqrt{3}$, and 2 are $(100)_c$, $(110)_c$, and $(200)_c$, respectively. On the other hand, the signatures of cubic double-gyroid structure are captured at q = 0.033 764 Å^{-1} ($q/q_g^* = 1$), 0.038 538 Å^{-1} ($q/q_g^* \cong (4/3)^{1/2}$), q = 0.061 007 Å^{-1} ($q/q_g^* \cong (10/3)^{1/2}$), q = 0.064 002 Å^{-1} ($q/q_g^* \cong (11/3)^{1/2}$), and 0.067 758 Å^{-1} ($q/q_g^* \cong 2$). The corresponding Miller indices for q/q_g^* = 1, $(4/3)^{1/2}$, $(10/3)^{1/2}$, $(11/3)^{1/2}$, 2 are $(112)_g$, $(0.24)_g$, $(233)_g$, and $(224)_g$, respectively.

On the basis of the evolution of Bragg peaks described above, we deduce that the disorder-to-order phase transition occurs at ~128 °C. The initial ordered structure is a hexagonal cylindrical structure. Further, an order−order transition occurs in the range 115−120 °C where coexistence of cubic double-gyroid and hexagonal cylindrical structure was observed. Theoretically,[16] the disordered state transition first to a body-centered cubic structure followed by an order−order transition from a body-centered cubic structure to a hexagonal cylindrical structure with decreasing temperature. However, experiments have found previously a direct transition from the disordered state to hexagonal cylindrical or lamella structures.[10] Here, we observe the direct transition from disordered state to hexagonal cylindrical structure.

The separation between the two peaks near q^* is only about 0.0003 Å^{-1}. As a result, SAXS facilities based at conventional X-ray sources and many synchrotron-based SAXS beamlines are not capable of resolving this double peak because of their coarser instrumental resolution than at 8-ID-I.[65] Careful examinations of the SAXS profiles over a wide range of wavevectors do not clearly reveal Bragg peaks, except near q/q^* = 2.0, suggesting that both the cubic double-gyroid and hexagonal cylindrical structures show significant local disorder.

Disordered-Phase Structure Factor. Figure 4a shows representative disordered-phase SAXS profiles of SI(10−16.5) at 130, 135, 140, and 150 °C. The experimental profiles are plotted as the open squares and the fitted profiles as the solid lines. We observe the expected single broad peak that diminishes in intensity with increasing temperature.[16−18,20] It is also evident that the peak wavevector, q^*, shifts to higher wavevectors with increasing temperature, similar to previous observations.[21,22,29,55,66−72] To quantify these data, we used a nonlinear least-squares fitting routine that implements Burger and Semenov's theoretical model,[20] incorporating polydispersity. Evidently, the fit provides an excellent description of the measured profiles. Five parameters, namely N, b, f, χ, and the polydispersity, U = PDI-1, were available to fit the SAXS profiles. Our initial guesses for N, b, f, and U were 418.32, 6.7 Å, 0.3468, and 0.09, respectively. The number-averaged polymerization index N is 418.32 in reference to a 100 Å^3 volume. The literature value for statistical segment length, b, is 6.7 Å for both polystyrene[73] and polyisoprene.[29] In a first round of fits, we allowed all five fitting parameters to vary. The resultant best fit values of N and b were 417.73 ± 3.82 and 6.50 ± 0.11 Å, respectively, nearly independent of temperatures. Therefore, we carried out a second round of fits, keeping the values of N and b fixed. The remaining three fitting parameters, f, U, and χ, were varied. Figure 4b shows the best fit values of χ versus T^{-1} (solid squares). Interestingly, with the procedure outlined, our fitted values of χ lie close to the form previously

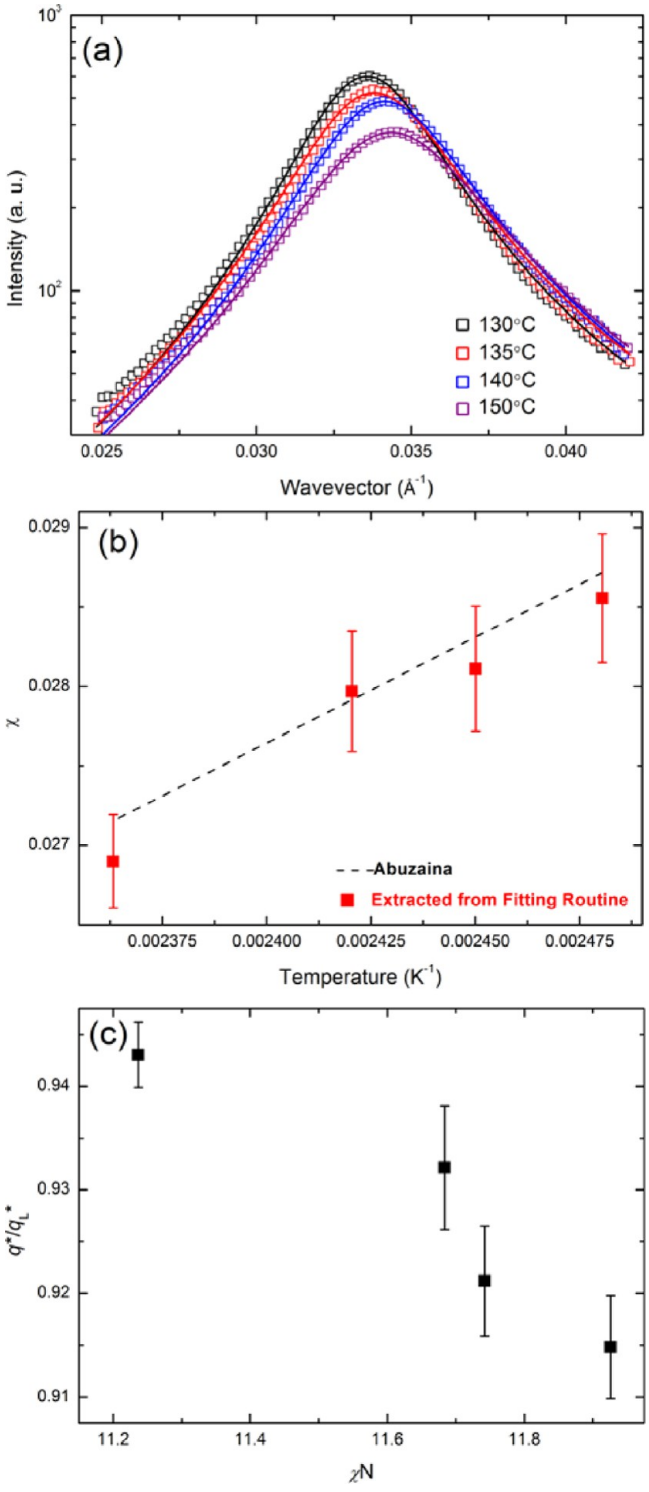

Figure 4. (a) SAXS profiles at 130, 135, 140, and 150 °C. The experimentally measured profiles are plotted as open squares, and the best fit to Burger and Semenov's model is plotted as the solid lines. (b) Molecular interaction parameter, χ, versus temperature, determined from our fits (solid symbols) compared to the functional form proposed by Abuzaina et al.[34] (c) Evolution of the measured normalized q^*/q^*_L with the fitted value of χN.

dx.doi.org/10.1021/ma4014548 | Macromolecules 2013, 46, 8628−8637

Table 1. Temperature Dependence of Parameters

temp (°C)	q^* (Å^{-1})	χ	f	U	τ^* (s)	τ(0.0036 Å^{-1}) (s)	D (Å^2/ms)	η (Pa·s)	R_H (nm)
128					3.281				
130	0.033 402	0.028 55	0.339 52	0.093 82	0.818	38.88	1.66	49.09	307.32
135	0.033 636	0.028 11	0.348 30	0.083 95	0.259	25.06	2.68	28.57	381.70
140	0.034 035	0.027 97	0.354 27	0.071 06	0.042	19.03	3.77	15.04	423.56
145								13.26	315.99
150	0.034 434	0.0269	0.377 82	0.052 49		7.26	9.50	10.90	297.05

reported by Abuzaina et al.,[34] which are shown as the dashed line. Abuzaina et al. found χ to be independent of copolymer composition, provided the minor block volume fraction is above 0.25, which they attributed to the absence of disordered micelles. Figure 4c plots the normalized peak wavevector, q^*/q_L^*, versus χN, where q_L^* is the peak wavevector, according to Leibler's theory, q_L^* = 0.036 513 Å for SI(10−16.5), and χN is determined from our fits. Glaser et al.[33] and Qin et al.[32] have presented theoretical and simulation results for q^* vs χN for a symmetric BCP, which show a similar variation. However, a direct comparison between this theory/simulation and our experiment is not possible because the range of values of χN studied theoretically[32,33] is from 0 to 10.5, whereas in our asymmetric BCP, χN varies between 11.2 and 12.7. Table 1 provides the temperature dependent parameters of current study.

We hypothesize that the best fits of χ, f, and U with changes in temperature describes the phase behavior of disordered SI(10−16.5) on the basis of Leibler's[16] and Semenov's[20] mean-field theory. However, accumulated theoretical[23,24,26,31−33,74] and experimental[10,29,40,55,68] studies attest a drawback of mean field theory and an importance of fluctuation effects. Furthermore, current SI(10−16.5) is relatively finite molecular weight. Thus, we acknowledge the limitation of mean field theory utilized in the present study.

Figure 5 presents the experimentally measured scattering profiles at 130, 135, 140, and 150 °C (open squares) from 0.004 to 0.07 Å^{-1}. In addition to strong scattering for wavevectors near q^*, these profiles also display strong scattering in the low wavevector range 0.004 Å^{-1} < q < 0.015 Å^{-1}. This component of the scattering certainly originates within the sample because removing the sample removes the scattering. Therefore, this excess scattering is not originated from a limitation of SAXS device. In addition, because the samples are annealed at 120 °C under vacuum for at least 12 h, we believe that it is unlikely that this component of the scattering originates with voids within the sample. However, an exposure to ambient air or thermal annealing may result in some degree of cross-linking or structural transition. Cross-linking or structural transition led to this component of scattering. Therefore, we performed the SEC experiments on as-received and thermal annealed SI(10−16.5) to monitor effects of thermal annealing and exposure to ambient air. Experimentally measure number- and weight-averaged molecular weight of as-received SI(10−16.5) are 17.459 ± 0.406 and 19.946 ± 0.211, respectively. Interestingly, experimentally measure number and weight-averaged molecular weight of thermal annealed SI(10−16.5) are 17.331 ± 0.027 and 19.806 ± 0.668, respectively. Therefore, the entire experimental procedure, including thermal annealing the exposure to ambient air, might not result in noticeable change of sample. However, small amounts of residual impurities are inevitable. Thus, small-angle neutron scattering (SANS) or ultrasmall-angle X-ray scattering possibly reveals the origin of mentioned excess scattering.

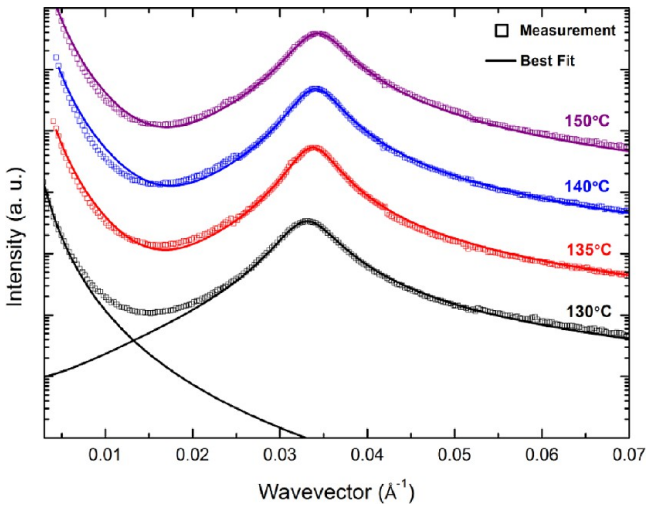

Figure 5. SAXS profiles in disordered phase plotted for wavevectors from 0.004 to 0.07 Å^{-1}. Open squares are the measured data, and the solid lines correspond to the best fits described in the text.

None of the previously mentioned theoretical models[16−18,20] can account for such strong scattering at low wavevectors. Therefore, to empirically model this scattering, we introduced the following form:[39]

$$S(q) = C/(1 + \varepsilon^4 q^4) \quad (4)$$

where C and ε are fitting parameters. To describe the SAXS profiles over the entire range of wavevectors studied, we fit the experimental profiles to the sum of eq 4 and the Burger and Semenov model. The fitting variables in this case were f, U, χ, ε, and C, with N and b remaining fixed. In fact, we found that only C/ε^4 was well determined, corresponding to large length scale fluctuations, beyond the instrumental resolution. This model accounts for the measured $S(q)$ quite well throughout the entire range of wavevectors, as shown by the solid lines in Figure 4. The best fit values of f, U, and χ are very similar to their values from fitting the more restricted range of wavevectors near the peak at q^*.

Disordered Phase Relaxations. XPCS measures the time correlation function of the SAXS intensity, $I(q,t)$:

$$g_2(q, t_d) \equiv \frac{\langle I(q, 0)I(q, t_d)\rangle}{\langle I(q, 0)\rangle^2} \quad (5)$$

The correlation function, g_2, decays with increasing delay time, t_d, and converges to unity at long time. The characteristic decay time (τ) reflects the structural dynamics of the sample, such as concentration fluctuations within the disordered state, dissolution and reappearance of micelles, or diffusion of intact micelles. To determine the characteristic relaxation times in the

dx.doi.org/10.1021/ma4014548 | Macromolecules 2013, 46, 8628−8637

context of SI(10−16.5), we represent eq 5 as a stretched exponential relaxation:

$$g_2 = 1 + A[g_1(q, t_d)]^2 \quad (6)$$

where A is the speckle contrast and $g_1(q,t_d) = \exp[-(t_d/\tau)^\beta]$ is the intermediate scattering function (ISF). Scattering signal is acquired as described elsewhere[75] and then fitted using simple ($\beta = 1$), stretched ($0 < \beta < 1$), or compressed ($\beta > 1$) exponential forms for the ISF.

We performed XPCS experiments on samples of SI(10−16.5) after annealing at 120 °C under vacuum for more than 12 h. In Figure 6a, we present measurements of g_2 obtained for three wavevectors, 0.032, 0.033, and 0.034 Å^{-1}, in the vicinity of q^*, at 128, 130, 135, and 140 °C. The open squares are the measured data, and the solid lines are nonlinear least-squares fits to eq 6, using the stretched exponential form. Each measurement shown in Figure 6a exhibits a relaxation and converges to unity with increasing delay time. Farther away from q^*, the lower SAXS intensity rendered the signal-to-noise ratio too low for meaningful measurements of g_2. For the measurements near q^* at 128 °C, g_2 falls from a value near 1.2 at 0.016 s to a value near 1 by 20 s. This gradual decay over 3 decades in time suggests stretched exponential behavior. At 128 °C, the characteristic decay time is in the 0.1−10 s range, but it decreases rapidly with increasing temperature. Nonlinear least-squares fitting of eq 6 to the data, with fitting parameters, A, β, and τ, provides a good description of the observed g_2s. To limit the number of fitting parameters, we decided to require the same value of A and β at all temperatures. Therefore, we fit the data by iteratively permuting the order of fitting the contrast (A) and stretching exponent (β) until convergence to stable values of A and β was reached. The values of A and β achieve in this way are $A = 0.242 \pm 0.017$ and $\beta = 0.360 \pm 0.027$. The value of β is indeed smaller than unity. Thus, SI(10−16.5) realizes stretched exponential relaxations.

Figure 6b displays $\ln(g_1^2)$ versus reduced the delay time:

$$\ln(g_1^2) = -2(t_d/\tau)^\beta \quad (7)$$

where t_d/τ is the reduced delay time. For the case of a simple exponential decay ($\beta = 1$), $\ln(g_1^2)$ versus reduced delay time curve is straight line with slope of −2, illustrated as the dashed line in Figure 6b. The experimental $\ln(g_1^2)$ curves at each temperature fall on top of one another, confirming a similar profile at each temperature. Strikingly, the experimental $\ln(g_1^2)$ curves exhibit a large positive curvature, corresponding to a stretched exponential decay $\beta = 0.360 \pm 0.027$. Such emphatically stretched exponential relaxations stand outside what is expected theoretically. Semenov et al.[44] and Mochrie[45] showed that compositional fluctuations in BCPs undergoing reptational motion are expected to decay as a sum of exponentials, which could in principle mimic stretched exponential relaxations. However, close to the MST, the theoretically predicted relaxations are dominated by a single exponential, which is not what we observe experimentally. The stretched exponential relaxations observed here are also different from the simple exponential relaxations, observed for highly asymmetric SI(7−27),[7,8] which suggests different dynamics in the two cases. Recently, similar stretching exponents have been reported in XPCS studies of dilute suspensions of gold nanoparticles, suspended in solutions of sufficiently high molecular weight ($M_w = 10^6$ g/mol) polystyrene homopolymer.[76] In that study, the stretched

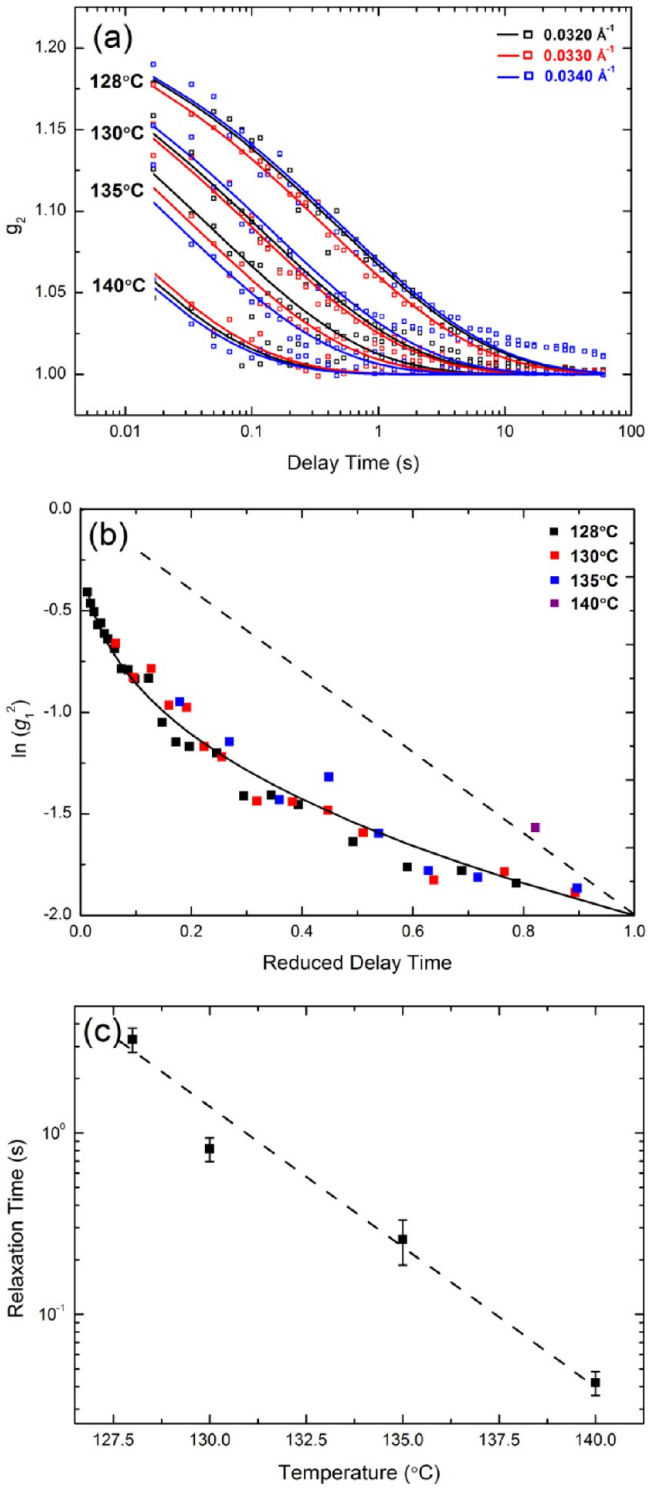

Figure 6. (a) Measured (symbols) and fitted (solid lines) intensity autocorrelations, g_2, plotted versus delay time at 128, 130, 135, and 140 °C for three wavevectors near the peak of the static scattering. (b) $\ln(g_1^2)$ versus reduced delay time. Strikingly, $\ln(g_1^2)$ plotted versus reduced delay time at each temperature exhibits a large positive curvature, indicating that relaxations follws a stretched exponential decay. (c) Mean structural relaxation time at q^*, determined from the fits shown in (a), plotted versus temperature (solid squares). The black dashed line is least-squares fits of τ^* to an exponential temperature dependence.

dx.doi.org/10.1021/ma4014548 | Macromolecules 2013, 46, 8628−8637

exponential relaxations were hypothesized to originate in nanoparticle hopping between polymer entanglement cages. Alternatively, if we hypothesize that the gold nanoparticles effectively label the polystyrene, and therefore report on the motion of the polymers, it follows that the process responsible for relaxations,[76] is analogous to the process by which compositional fluctuations in entangled BCP are envisioned to relax. It would then be natural for both systems to show similar stretched exponential relaxations.

The black solid squares in Figure 6c correspond to the mean structural relaxation time averaged over all wavevectors, 0.032, 0.033, and 0.034 Å^{-1}. The error bars represent the standard deviation of these averaged values. The dashed line in Figure 6c corresponds to

$$\tau^* = \Gamma \exp[-\Delta T\ (^\circ\mathrm{C})/2.96] \quad (8)$$

where τ^* is the relaxation time at q^*, $\Gamma = \tau(q = q^*, T = 140\ ^\circ\mathrm{C})$, and $\Delta T = T - 140\ ^\circ\mathrm{C}$, which satisfactorily describes the temperature dependence of the structural relaxation time at q^*.

We also investigated the dynamics of the excess scattering at low wavevectors. Figure 7a shows representative g_2 profiles obtained at $q = 0.0044$ Å^{-1} for 130, 135, 140, and 150 °C (open squares). It is clear from this figure that the scattering at low wavevectors is dynamic with a temperature-dependent relaxation time that decreases with increasing temperature. Similarly to the analysis described above, we fit these data to eq 6. Initial fitting revealed that the data are well described by $\beta = 1$ and a fixed value of A, and so we used a simple exponential decay, $g_2 = 1 + Ae^{-2(t_d/\tau)}$ with $A = 0.227 \pm 0.014$. The corresponding best fit values of the relaxation time are plotted versus temperature in Figure 7b for 0.0036, 0.0044, and 0.0052 Å^{-1}. The temperature dependence of τ is well described as an exponential at all wavevectors studied, as shown by the dashed lines in Figure 7, which correspond to the form

$$\tau = \Gamma_L \exp[-\Delta T\ (^\circ\mathrm{C})/11.4] \quad (9)$$

where $\Gamma_L = \tau(q \leq 0.0052$ Å^{-1}, $T = 130\ ^\circ\mathrm{C})$ and $\Delta T = T - 130\ ^\circ\mathrm{C}$. Equations 8 and 9 differ in the rapidity of the temperature variation: the relaxation time at q^* varies by a factor of 2 for each 2.0 °C change in temperature, while the relaxation time at low wavevectors varies by a factor of 2 for each 7.9 °C change in temperature. The different relaxation functions and different temperature dependences at low wavevectors and wavevector near q^* surely reflect that different processes are relevant at different length scales: fluid flow at low wavevectors, corresponding to relatively large distances, and concentration fluctuations at q^*, corresponding to relatively short distances.

Figure 8 plots τ^{-1} vs q^2 at each temperature, showing a more-or-less linear relationship, as expected for diffusive relaxations. Specifically, we expect $\tau^{-1} = Dq^2$, where D is the diffusion coefficient. According to the Stokes–Einstein relation, the hydrodynamic radius (R_H) of the diffusing objects is

$$D = \frac{k_B T}{6\pi\eta R_H} \quad (10)$$

where k_B is Boltzmann's constant and η is the viscosity. To test whether the relaxation time at low wavevectors is determined by the macroscopic viscosity and to ascertain the corresponding value of R_H, we measured the macroscopic viscosity of SI(10–16.5). Specifically, SI(10–16.5) BCP was subjected to dynamic frequency sweeps from 0.1 to 100 rad s^{-1} within the linear viscoelastic regime at 130, 135, 140, 145, and 150 °C using an

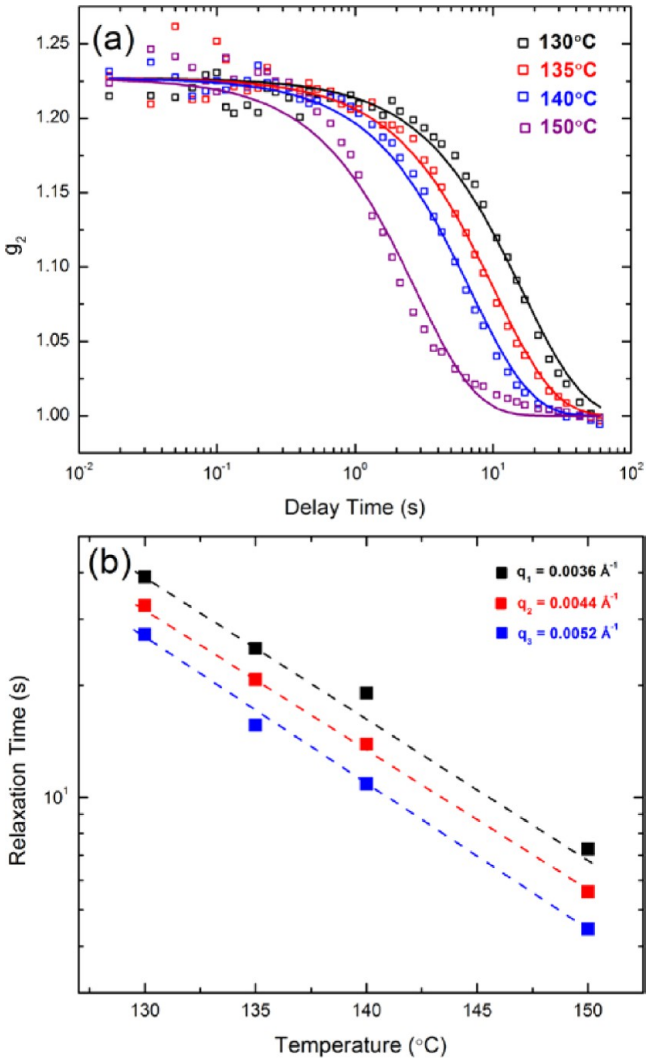

Figure 7. (a) Representative intensity autocorrelations, g_2, plotted versus delay time at $q = 0.0044$ Å^{-1} for 130, 135, 140, and 150 °C. (b) Relaxation time plotted versus temperature for $q = 0.0036$, 0.0044, and 0.0052 Å^{-1}. The dashed lines are least-squares fits of τ to an exponential temperature dependence (eq 4).

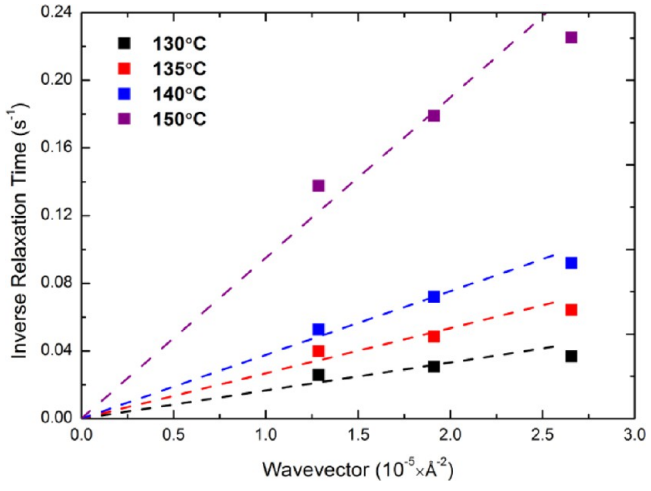

Figure 8. Inverse relaxation time, τ^{-1} (solid squares), plotted versus the square of the wavevector, q^2, for 130, 135, 140, and 150 °C.

dx.doi.org/10.1021/ma4014548 | Macromolecules 2013, 46, 8628–8637

ARES-LS1 viscometer. The resultant macroscopic viscosity at each temperature together with the corresponding values of R_H is given in Table 1. Remarkably, the values of R_H determined from eq 10 are approximately 350 nm at all temperatures with an average of 345.1 ± 55.0 nm. This observation confirms that the temperature dependence of the low-wavevector relaxations is the same as that of the macroscopic viscosity within errors. In addition, such a large value of R_H is consistent with the static scattering, for which we found that the length scale, ε (eq 4), was larger than could be resolved.

CONCLUSIONS

We have presented a SAXS and XPCS study of the static and dynamic behavior of a poly(styrene-*b*-isoprene) diblock copolymer melt with a styrene volume fraction of 0.35. Microphase separation transition and order−disorder temperature was successfully monitored using temperature-controlled SAXS. Immediately below the microphase separation transition, which is located near 128 °C, we observed the peaks at $q/q^* \cong \sqrt{3}$ and 2 at 125 °C. These peaks originate from hexagonally packed cylindrical structure. Further, we observe a presumable coexistence of two different structures at 120 and 115 °C. On the basis of its predicted small splitting of the principal Bragg peak near $q/q^* = 1$, which has not previously been reported as far as we are aware, coexistence of two different morphology was strikingly revealed. This observation exemplifies how high-resolution synchrotron X-ray measurements can easily reveal structural details that would not be resolvable by conventional SAXS. This coexistence is supported by the speckle pattern from 2D CCD images and SAXS intensity profiles.

In the disordered phase, above 130 °C, we have characterized the dynamics of composition fluctuations via X-ray photon correlation spectroscopy (XPCS). Near the peak of the static structure factor, these fluctuations show strongly stretched-exponential relaxations, characterized by a stretching exponent of 0.36 for a range of temperatures above the microphase separation transition. The corresponding characteristic relaxation times vary very rapidly with temperature, changing by a factor of 2 for each 2 °C change in temperature. Recently, similar stretching exponents have been reported in XPCS studies of dilute suspensions of gold nanoparticles, suspended in solutions of high molecular weight homopolymer,[76] suggesting that similar relaxation mechanisms may operate in both systems. Unfortunately, in the present experiment, the signal-to-noise ratio for wavevectors away from the peak of the structure factor was too low to determine the characteristic relaxation times away from the peak. A similar limitation was found in the study of SI(7−27) by Patel et al. XPCS studies of block copolymer dynamics at moderate wavevectors away from q^* will likely have to await future experiments at still brighter X-ray sources.

We also characterized the excess scattering at low wavevectors that appears ubiquitously in scattering experiments on polymer systems. In this case, the measured relaxations are diffusive with relaxation times that change by a factor of 2 for each 8 °C change in temperature, which is similar to the measured temperature dependence of the macroscopic viscosity of SI(10−16.5). The different relaxation functions and different temperature dependences for the low- and high-wavevector relaxations indicate that different processes are responsible in each case. Assuming that the low-wavevector dynamics correspond to diffusion through a fluid with the macroscopic viscosity of SI(10−16.5), the hydrodynamic radius of the diffusing objects is calculated to be about 350 nm. This large length scale is consistent with the SAXS intensity observed at low wavectors, which cannot resolve the length scale associated with the low-wavevector excess scattering. Although this scattering must be the result of long length scale inhomogeneities within the sample, its specific origin remains uncertain. Nevertheless, we have shown that such scattering may serve as a useful proxy for the sample's macroscopic viscosity in XPCS experiments. With the deliberate addition of well-defined, large probe particles, all uncertainly in R_H could be removed, and it might be possible to unambiguously compare microscopic and macroscopic dynamics in one XPCS experiment.

AUTHOR INFORMATION

Corresponding Author

*E-mail: simon.mochrie@yale.edu (S.G.J.M.).

Notes

The authors declare no competing financial interest.

ACKNOWLEDGMENTS

This work was supported by the DOE Division of Basic Energy Sciences under Grant DE-SC0004162. Use of the Advanced Photon Source, an Office of Science User Facility operated for the U.S. Department of Energy (DOE) Office of Science by Argonne National Laboratory, was supported by the U.S. DOE under Contract DE-AC02-06CH11357. We thank C. Osuji and Z. Shao for valuable discussions and assistance.

REFERENCES

(1) Duong, P. H. H.; Chung, T. S.; Jeyaseelan, K.; Armugam, A.; Chen, Z. C.; Yang, J.; Hong, M. H. *J. Membr. Sci.* **2012**, *409*, 34−43.
(2) Gu, Y. Y.; Lodge, T. P. *Macromolecules* **2011**, *44* (7), 1732−1736.
(3) Jha, A. K.; Chen, L.; Offeman, R. D.; Balsara, N. P. *J. Membr. Sci.* **2011**, *373* (1−2), 112−120.
(4) Schauer, J.; Llanos, J.; Zitka, J.; Hnat, J.; Bouzek, K. *J. Appl. Polym. Sci.* **2012**, *124*, E66−E72.
(5) Oh, H.; Green, P. F. *Macromolecules* **2008**, *41* (7), 2561−2566.
(6) Kim, S. S.; Choi, J. Y.; Kim, K.; Sohn, B. H. *Nanotechnology* **2012**, *23*, 12.
(7) Patel, A. J.; Narayanan, S.; Sandy, A.; Mochrie, S. G. J.; Garetz, B. A.; Watanabe, H.; Balsara, N. P. *Phys. Rev. Lett.* **2006**, *96* (25), 257801.
(8) Patel, A. J.; Mochrie, S.; Narayanan, S.; Sandy, A.; Watanabe, H.; Balsara, N. P. *Macromolecules* **2010**, *43* (3), 1515−1523.
(9) Hajduk, D. A.; Harper, P. E.; Gruner, S. M.; Honeker, C. C.; Kim, G.; Thomas, E. L.; Fetters, L. J. *Macromolecules* **1994**, *27* (15), 4063−4075.
(10) Khandpur, A. K.; Forster, S.; Bates, F. S.; Hamley, I. W.; Ryan, A. J.; Bras, W.; Almdal, K.; Mortensen, K. *Macromolecules* **1995**, *28* (26), 8796−8806.
(11) Epps, T. H.; Cochran, E. W.; Bailey, T. S.; Waletzko, R. S.; Hardy, C. M.; Bates, F. S. *Macromolecules* **2004**, *37* (22), 8325−8341.
(12) Tyler, C. A.; Morse, D. C. *Phys. Rev. Lett.* **2005**, *94* (20), 208302.
(13) Yamada, K.; Nonomura, M.; Ohta, T. *J. Phys.: Condens. Matter* **2006**, *18* (32), L421−L427.
(14) Ranjan, A.; Morse, D. C. *Phys. Rev. E* **2006**, *74* (1), 011803.
(15) Takenaka, M.; Wakada, T.; Akasaka, S.; Nishitsuji, S.; Saijo, K.; Shimizu, H.; Kim, M. I.; Hasegawa, H. *Macromolecules* **2007**, *40* (13), 4399−4402.
(16) Leibler, L. *Macromolecules* **1980**, *13* (6), 1602−1617.
(17) Fredrickson, G. H.; Helfand, E. *J. Chem. Phys.* **1987**, *87* (1), 697−705.
(18) Leibler, L.; Benoit, H. *Polymer* **1981**, *22* (2), 195−201.
(19) Hong, K. M.; Noolandi, J. *Polym. Commun.* **1984**, *25* (9), 265−268.

(20) Burger, C.; Ruland, W.; Semenov, A. N. *Macromolecules* **1990**, *23* (13), 3339−3346.
(21) Lin, C. C.; Jonnalagadda, S. V.; Kesani, P. K.; Dai, H. J.; Balsara, N. P. *Macromolecules* **1994**, *27* (26), 7769−7780.
(22) Bartels, V. T.; Abetz, V.; Mortensen, K.; Stamm, M. *Europhys. Lett.* **1994**, *27* (5), 371−376.
(23) Fried, H.; Binder, K. *J. Chem. Phys.* **1991**, *94* (12), 8349−8366.
(24) Murat, M.; Grest, G. S.; Kremer, K. *Macromolecules* **1999**, *32* (3), 595−609.
(25) Carmesin, I.; Kremer, K. *Macromolecules* **1988**, *21* (9), 2819−2823.
(26) Muller, M.; Binder, K. *Macromolecules* **1995**, *28* (6), 1825−1834.
(27) Kremer, K.; Grest, G. S. *J. Chem. Phys.* **1990**, *92* (8), 5057−5086.
(28) Almdal, K.; Rosedale, J. H.; Bates, F. S.; Wignall, G. D.; Fredrickson, G. H. *Phys. Rev. Lett.* **1990**, *65* (9), 1112−1115.
(29) Bates, F. S.; Hartney, M. A. *Macromolecules* **1985**, *18* (12), 2478−2486.
(30) Wang, J. F.; Wang, Z. G.; Yang, Y. L. *Macromolecules* **2005**, *38* (5), 1979−1988.
(31) Qin, J.; Grzywacz, P.; Morse, D. C. *J. Chem. Phys.* **2011**, *135* (8), 084902.
(32) Qin, J.; Morse, D. C. *Phys. Rev. Lett.* **2012**, *108* (23), 238301.
(33) Glaser, J.; Qin, J.; Medapuram, P.; Muller, M.; Morse, D. C. *Soft Matter* **2012**, *8* (44), 11310−11317.
(34) Abuzaina, F. M.; Patel, A. J.; Mochrie, S.; Narayanan, S.; Sandy, A.; Garetz, B. A.; Balsara, N. P. *Macromolecules* **2005**, *38* (16), 7090−7097.
(35) Tonami, K.; Nojima, S.; Honda, T.; Tsunogae, Y. *Polym. J.* **2009**, *41* (12), 1041−1048.
(36) Hsiao, B. S.; Gardner, K. H.; Wu, D. Q.; Chu, B. *Polymer* **1993**, *34* (19), 3996−4003.
(37) Kruger, K. N.; Zachmann, H. G. *Macromolecules* **1993**, *26* (19), 5202−5208.
(38) Wang, Z. G.; Wang, X. H.; Hsiao, B. S.; Phillips, R. A.; Medellin-Rodriguez, F. J.; Srinivas, S.; Wang, H.; Han, C. C. *J. Polym. Sci., Part B: Polym. Phys.* **2001**, *39* (23), 2982−2995.
(39) Koberstein, J. T.; Picot, C.; Benoit, H. *Polymer* **1985**, *26* (5), 673−681.
(40) Karatasos, K.; Anastasiadis, S. H.; Semenov, A. N.; Fytas, G.; Pitsikalis, M.; Hadjichristidis, N. *Macromolecules* **1994**, *27* (13), 3543−3552.
(41) Lodge, T. P.; Hamersky, M. W.; Milhaupt, J. M.; Kannan, R. M.; Dalvi, M. C.; Eastman, C. E. *Macromol. Symp.* **1997**, *121*, 219−233.
(42) Fleischer, G.; Fujara, F.; Stuhn, B. *Macromolecules* **1993**, *26* (9), 2340−2345.
(43) Brochard, F.; de Gennes, P. G. *Physica A* **1983**, *118*, 289−299.
(44) Semenov, A. N.; Anastasiadis, S. H.; Boudenne, N.; Fytas, G.; Xenidou, M.; Hadjichristidis, N. *Macromolecules* **1997**, *30* (20), 6280−6294.
(45) Mochrie, S. G. J. *Macromolecules* **2003**, *36* (13), 5013−5019.
(46) Fredrickson, G. H.; Larson, R. G. *J. Chem. Phys.* **1987**, *86* (3), 1553−1560.
(47) Mochrie, S. G. J.; Mayes, A. M.; Sandy, A. R.; Sutton, M.; Brauer, S.; Stephenson, G. B.; Abernathy, D. L.; Grubel, G. *Phys. Rev. Lett.* **1997**, *78* (7), 1275−1278.
(48) Dierker, S. B.; Pindak, R.; Fleming, R. M.; Robinson, I. K.; Berman, L. *Phys. Rev. Lett.* **1995**, *75* (3), 449−452.
(49) Li, C. H.; Koga, T.; Jiang, J.; Sharma, S.; Narayanan, S.; Lurio, L. B.; Hu, Y.; Jiao, X.; Sinha, S. K.; Billet, S.; Sosnowik, D.; Kim, H.; Sokolov, J. C.; Rafailovich, M. H. *Macromolecules* **2005**, *38* (12), 5144−5151.
(50) Brinker, K. L.; Mochrie, S. G. J.; Burghardt, W. R. *Macromolecules* **2007**, *40* (14), 5150−5160.
(51) Falus, P.; Borthwick, M. A.; Mochrie, S. G. J. *Rev. Sci. Instrum.* **2004**, *75* (11), 4383−4400.
(52) Falus, P.; Lurio, L. B.; Mochrie, S. G. J. *J. Synchrotron Radiat.* **2006**, *13*, 253−259.
(53) Barrere, C.; Mazarin, M.; Giordanengo, R.; Phan, T. N. T.; Thevand, A.; Viel, S.; Charles, L. *Anal. Chem.* **2009**, *81* (19), 8054−8060.
(54) Lumma, D.; Lurio, L. B.; Mochrie, S. G. J.; Sutton, M. *Rev. Sci. Instrum.* **2000**, *71* (9), 3274−3289.
(55) Almdal, K.; Bates, F. S.; Mortensen, K. *J. Chem. Phys.* **1992**, *96* (12), 9122−9132.
(56) Winter, H. H.; Scott, D. B.; Gronski, W.; Okamoto, S.; Hashimoto, T. *Macromolecules* **1993**, *26* (26), 7236−7244.
(57) Habersberger, B. M.; Bates, F. S.; Lodge, T. P. *Soft Matter* **2012**, *8* (12), 3429−3441.
(58) Mogi, Y.; Nomura, M.; Kotsuji, H.; Ohnishi, K.; Matsushita, Y.; Noda, I. *Macromolecules* **1994**, *27* (23), 6755−6760.
(59) Hajduk, D. A.; Gruner, S. M.; Rangarajan, P.; Register, R. A.; Fetters, L. J.; Honeker, C.; Albalak, R. J.; Thomas, E. L. *Macromolecules* **1994**, *27* (2), 490−501.
(60) Ryu, C. Y.; Lee, M. S.; Hajduk, D. A.; Lodge, T. P. *J. Polym. Sci., Part B: Polym. Phys.* **1997**, *35* (17), 2811−2823.
(61) Epps, T. H.; Cochran, E. W.; Hardy, C. M.; Bailey, T. S.; Waletzko, R. S.; Bates, F. S. *Macromolecules* **2004**, *37* (19), 7085−7088.
(62) Avgeropoulos, A.; Dair, B. J.; Hadjichristidis, N.; Thomas, E. L. *Macromolecules* **1997**, *30* (19), 5634−5642.
(63) Suzuki, J.; Seki, M.; Matsushita, Y. *J. Chem. Phys.* **2000**, *112* (10), 4862−4868.
(64) Forster, S.; Khandpur, A. K.; Zhao, J.; Bates, F. S.; Hamley, I. W.; Ryan, A. J.; Bras, W. *Macromolecules* **1994**, *27* (23), 6922−6935.
(65) Saranathan, V.; Osuji, C. O.; Mochrie, S. G. J.; Noh, H.; Narayanan, S.; Sandy, A.; Dufresne, E. R.; Prum, R. O. *Proc. Natl. Acad. Sci. U. S. A.* **2010**, *107* (26), 11676−11681.
(66) Owens, J. N.; Gancarz, I. S.; Koberstein, J. T.; Russell, T. P. *Macromolecules* **1989**, *22* (8), 3388−3394.
(67) Maurer, W. W.; Bates, F. S.; Lodge, T. P.; Almdal, K.; Mortensen, K.; Fredrickson, G. H. *J. Chem. Phys.* **1998**, *108* (7), 2989−3000.
(68) Bates, F. S.; Rosedale, J. H.; Fredrickson, G. H. *J. Chem. Phys.* **1990**, *92* (10), 6255−6270.
(69) Rosedale, J.; Bates, F. S.; Almdal, K.; Mortensen, K.; Wignall, G. D. *Macromolecules* **1995**, *28* (5), 1429−1443.
(70) Wolff, T.; Burger, C.; Ruland, W. *Macromolecules* **1993**, *26* (7), 1707−1711.
(71) Stuhn, B.; Mutter, R.; Albrecht, T. *Europhys. Lett.* **1992**, *18* (5), 427−432.
(72) Mori, K.; Hasegawa, H.; Hashimoto, T. *Polymer* **2001**, *42* (7), 3009−3021.
(73) Bates, F. S.; Wignall, G. D. *Phys. Rev. Lett.* **1986**, *57* (12), 1429−1432.
(74) Grzywacz, P.; Qin, J.; Morse, D. C. *Phys. Rev. E* **2007**, *76* (6), 061802.
(75) Falus, P.; Narayanan, S.; Sandy, A. R.; Mochrie, S. G. J. *Phys. Rev. Lett.* **2006**, *97* (6), 066102.
(76) Guo, H.; Bourret, G.; Lennox, R. B.; Sutton, M.; Harden, J. L.; Leheny, R. L. *Phys. Rev. Lett.* **2012**, *109* (5), 055901.